Biochar

ORIGINAL RESEARCH

Wood-derived biochar as thick electrodes for high-rate performance supercapacitors

Bing Yan[1], Jiaojiao Zheng[1], Li Feng[1], Cheng Du[2,3], Shaoju Jian[4], Weisen Yang[4], Yimin A. Wu[3*], Shaohua Jiang[1], Shuijian He[1*] and Wei Chen[2,5*]

Abstract

Developing effective electrodes with commercial-level active mass-loading (> 10 mg cm^{-2}) is vital for the practical application of supercapacitors. However, high active mass-loading usually requires thick active mass layer, which severely hinders the ion/electron transport and results in poor capacitive performance. Herein, a self-standing biochar electrode with active mass-loading of ca. 40 mg cm^{-2} and thickness of 800 µm has been developed from basswood. The basswood was treated with formamide to incorporate N/O in the carbon structure, followed by mild KOH activation to ameliorate the pore size and introduce more O species in the carbon matrix. The as-prepared carbon monoliths possess well conductive carbon skeleton, abundant N/O dopant and 3D porous structure, which are favorable for the ion/electron transport and promoting capacitance performance. The self-standing carbon electrode not only exhibits the maximum areal/mass/volumetric specific capacitance of 5037.5 mF cm^{-2}/172.5 F g^{-1}/63.0 F cm^{-3} at 2 mA cm^{-2} (0.05 A g^{-1}), but also displays excellent rate performance with 76% capacitance retention at 500 mA cm^{-2} (12.5 A g^{-1}) in a symmetric supercapacitor, surpassing the state-of-art biomass-based thick carbon electrode. The assembled model can power typical electron devices including a fan, a digital watch and a logo made up of 34 light-emitting diodes for a proper period, revealing its practical application potential. This study not only puts forward a commercial-level high active mass-loading electrode from biomass for supercapacitor, but also bridges the gap between the experimental research and practical application.

Article Highlights

- Basswood-derived free-standing thick carbon electrodes were developed for supercapacitors.
- The capacitance performance was enhanced by pre-oxidation, solvothermal treatment and KOH activation.
- Supercapacitors assembled from the optimized electrode exhibited good rate performance and stability.

*Correspondence: yimin.wu@uwaterloo.ca; shuijianhe@njfu.edu.cn; weichen@ciac.ac.cn

[1] International Innovation Center for Forest Chemicals and Materials, Co-Innovation Center of Efficient Processing and Utilization of Forest Resources, College of Materials Science and Engineering, Nanjing Forestry University, Nanjing 210037, China
[2] State Key Laboratory of Electroanalytical Chemistry, Changchun Institute of Applied Chemistry, Chinese Academy of Sciences, Changchun 130022, Jilin, People's Republic of China
[3] Department of Mechanical and Mechatronics Engineering Waterloo Institute of Nanotechnology, University of Waterloo, Waterloo, ON N2L 3G1, Canada
Full list of author information is available at the end of the article

Springer

Keywords: Biochar, High mass-loading, Heteroatom doping, Self-standing electrodes, Supercapacitor

Graphical abstract
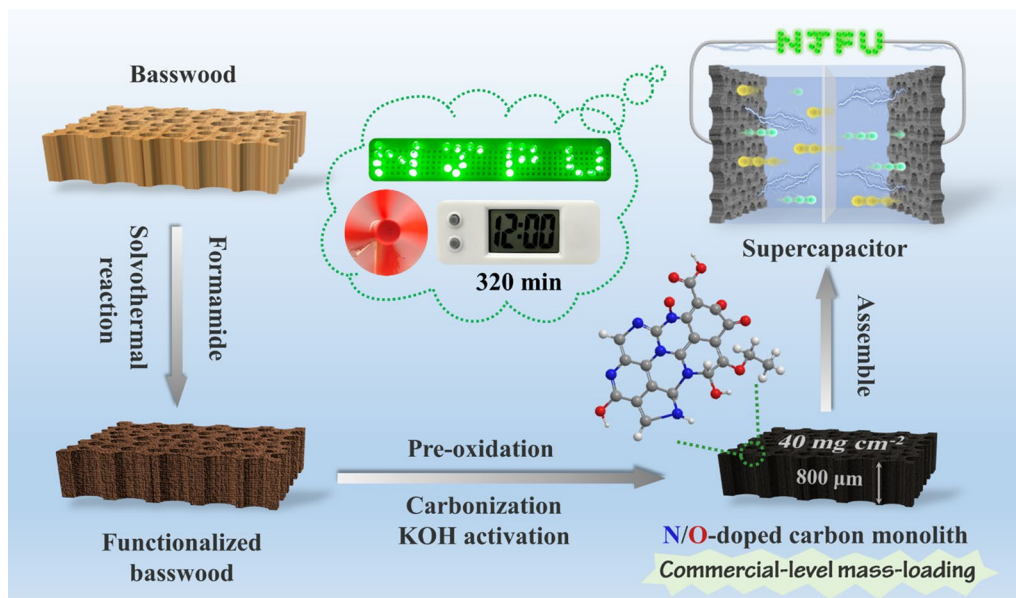
1 Introduction

Faced with the increasingly serious energy crisis and climate change, a huge effort has been contributed to the "carbon-neutral" energy storage technologies. Supercapacitors, especially electric double layer capacitors (EDLCs), show great potential in next-generation energy storage and supply technology attributing to their multiple advantages such as low cost/contamination, rapid charge/discharge capabilities, long lifespan and outstanding power density (Su et al. 2022; Katsuyama et al. 2022). In EDLCs, the charge is stored/released through the adsorption/desorption of electrolyte ions at the interface of electrode materials (Zheng et al. 2021a; Liu et al. 2022b; Wang et al. 2022a). Therefore, electrode materials with superior ion/electron transport channels play a critical role in determining the energy storage/release capacity of SCs. Following this principle, researchers have developed a large number of porous carbon electrodes with seemingly excellent capacitive performance in the laboratory (Wang et al. 2021f; Guo et al. 2021). However, those apparently high capacitive performances can only be achieved on very thin layer with low active mass-loading (2–3 mg cm^{-2}), which is far from the commercial requirement (>10 mg cm^{-2}), and the capacitance performance of the materials may be overestimated due to low active mass-loading (Dong et al. 2020; Boyce et al. 2021). The low mass loading also results in high mass ratio of inactive components (including the current collector, membrane, electrolyte, package, etc.), considerably impeding the development of high energy density, lightweight, and low-cost supercapacitors. Crucially, increasing the active mass loading always results in rapid fading of specific capacitance and rate performance due to the decreased accessible surface area, enlarged electrical resistance and prolonged charge/ion transport channels. When the active mass loading increases from laboratory grade to commercial level, the capacitance decreases by at least 10% or even more than 50% (Huang et al. 2019b; Zhao et al. 2020). Thus, it is urgent and meaningful to develop high active mass-loading EDLCs while maintaining the high capacitive performance.

To bridge the gap between the experimental results and practical applications, versatile methods have been developed, which can be classified into the "bottom-up" and "top-down" strategies (Kuang et al. 2019; He et al. 2020; Wu et al. 2021). The "bottom-up" strategy is accustomed to utilizing high conductive low dimensional carbon nanomaterials (such as carbon nanotubes (CNTs), graphene oxide (GO), graphene quantum dots (GQDs), etc.) as conductive additives to construct outer conductive networks between activated carbon particles (Zhang et al. 2019b; Chen et al. 2021b). In addition, the basic structural units (CNTs, GO, MXene) can also serve as electrodes with inner conductive networks via

various methods such as micelle-induced assembly (Tian et al. 2020), electrophoretic deposition (Chang and Hu 2019), wet-spinning (Huang et al. 2019b), vacuum filtration (Zheng et al. 2021c), mechanical compression (Plaza-Rivera et al. 2020) and so on. Although high active mass-loading could be achieved through such "bottom-up" strategies, the complexities and/or cost of some strategies render them impractical. Besides, the inevitable agglomeration or entanglement of those structural units induced by π–π interaction or capillary effect not only causes uneven distribution of charges in the electrodes but also increases the diffusion resistance of electrolyte ions, resulting in poor ion/electron transport dynamics and decayed capacitance performance. In contrast, the "top-down" strategies show great potential in constructing commercial-level active mass loading electrodes with interconnected porous structure and abundant active sites, taking advantage of templates [such as metal-based nanoparticles (Wang et al. 2021a), block copolymer (Liu et al. 2019b), ice crystals, laser patterning (Dubey et al. 2020), etc.], active site design (heteroatom doping) (Zhao et al. 2020), and physical/chemical activation (Chen et al. 2021c).

Among a variety of carbonaceous precursors, the renewable basswood blocks are the promising choice. Basswood with elaborate hierarchically porous structure (such as vertical vessels/tracheids, numerous pits and nanopores) has evolved over hundreds of millions of years on the earth, which was very suitable for mass transfer, and its anisotropic structure could be well inherited after carbonization. Their vertical channels act as electrolyte buffer pools to shorten the diffusion distance of electrolyte ions, and the penetrating pits on the channel walls provide paths for electrolyte transfer between adjacent channels. In addition, their integral self-supporting structure avoids excessive interfacial resistance that is detrimental to capacitance performance, and the long-range and ordered conductive framework of the carbonized sample is beneficial for electrons transfer (Wang et al. 2021d, 2021e; Qing et al. 2021). In addition, the main components of basswood (cellulose, hemicellulose, and lignin) contain numerous active functional groups (like –OH, –COOH, etc.), which favors the combination with dopants (Chen et al. 2020; Xia et al. 2020; Wang et al. 2021g; Xiao et al. 2022). Therefore, utilizing basswood as the precursor to improve surface chemistry and pore properties of the resulted free-standing thick carbon electrode is a more energy-efficient "top-down" method.

Herein, we successfully prepared a self-standing N/O co-doped biochar electrode with high active mass-loading of ca. 40 mg cm^{-2} and thickness of 800 μm. Owing to the ingenious synthesis procedure, the basswood derived self-standing electrodes possess well-tuned 3D porous structure and abundant N/O dopant, which endow the electrodes excellent capacitive performance even though at such high active mass-loading. Specifically, the maximum areal, volumetric and gravimetric specific capacitance of the obtained electrodes achieved 6538.5 mF cm^{-2}, 81.7 F cm^{-3} and 223.9 F g^{-1} at 2 mA cm^{-2} (0.05 F g^{-1}), respectively, along with a prominent rate capability of 3821.2 mF cm^{-2}, 47.8 F cm^{-3} and 130.9 F g^{-1} even at 500 mA cm^{-2} (12.50 F g^{-1}). Moreover, the symmetric supercapacitors exhibited preferable power density (58.0 mW cm^{-2}, 1996.4 W kg^{-1} and 725.0 mW cm^{-3}) and energy density (0.65 mWh cm^{-2}, 8.15 mWh cm^{-3} and 22.44 Wh kg^{-1}) compared to other state-of-art biomass-based thick electrode supercapacitors. The assembled model even can power typical electron devices including a fan, a digital watch and a logo made up of 34 light-emitting diodes for a proper period, revealing its practical application potential.

2 Experimental
2.1 Materials
Basswood was supplied by Chenlin Industrial Co., Ltd. Formamide (FA, Rhawn Co. Ltd), potassium hydroxide (KOH, Sinopharm Co. Ltd), ethanol (95%, Sinopharm Co. Ltd) and hydrochloric acid (HCl, 36%, Nanjing Chemical Reagent Co., Ltd.) were of analytical grade and used without further purification. Ultrapure water (18.2 MΩ cm) was used throughout the experiment.

2.2 Preparation of FA-OC slices
Basswood blocks (W) were cross-cut into veneers with the size of 2 cm × 1.5 cm × 0.1 cm. Specifically, five pieces of basswood were immersed into 60 mL formamide (FA) for 30 min and then transferred into a 100 mL Teflon-lined stainless-steel autoclave. The sealed Teflon-lined autoclave was maintained at 120 °C for 3 h and heated to 180 °C for 2 h. After the reaction, the autoclave was cooled naturally. The solvothermal treated basswood pieces were taken out, washed with pure water and dried in an oven at 60 °C overnight. The obtained samples were named FA-W. The FA-W slices were pre-oxidized at 260 °C for 6 h under air flow (200 sccm) and then carbonized at 1000 °C for 2 h under N$_2$ atmosphere (100 sccm) in a tube furnace, and the heating rate for both pre-oxidation and carbonization was 5 °C min^{-1}. Finally, the obtained carbon materials were denoted as FA-OC. In contrast, the carbonaceous product obtained from directly carbonization of basswood was labeled as WC, and the sample obtained from carbonization of the

pre-oxidized basswood without FA treatment was abbreviated as OC.

2.3 Preparation of KOH activated FA-OC slices
Typically, the FA-OC slices were immersed into the 200 mM KOH ethanol solution for 48 h to ensure sufficient penetration of the activator. FA-OC slices loaded with KOH were placed in an oven at 60 °C to completely volatilize the ethanol. The dried samples were placed into a tube furnace and activated at 800 °C (heating rate of 5 °C min^{-1}) for 2 h under N_2 flow (100 sccm). The carbonized wood slices were immersed in 1 M HCl solution for 12 h to remove potential inorganic residues, and rinsed with pure water until pH of the filtrate closed to 7. The dried samples were denoted as FA-OC2. Additionally, other samples were prepared by varying the concentration of KOH ethanol solution (100 mM and 300 mM), which were labeled as FA-OC1 and FA-OC3, respectively.

2.4 Material characterization
The attenuated total reflectance Fourier-transform infrared spectroscopy (ATR-FTIR, VERTEX 80V) was used to collect IR spectra to confirm the functional groups in the functionalized basswood. The morphologies of the basswood-derived carbon materials were characterized by scanning electron microscopy (SEM; JSM-7600F) at an acceleration voltage of 15 kV. Elemental mapping was determined by an energy-dispersive X-ray spectroscopy (EDS, INCA X-Act). The high-resolution transmission electron microscope (HRTEM, JEM-2100 UHR) and selected area electron diffraction (SAED) images were acquired at an accelerating voltage of 200 kV. Thermogravimetric analyses (TGA, NETZSCH TG 209F3) were investigated with a heating rate of 10 °C min^{-1} in N_2 atmosphere to analyze the thermal decomposition of samples. X-ray diffraction (XRD, Ultima IV) patterns of samples were measured at a voltage of 40 kV and a current of 30 mA, employing a scanning rate 10° min^{-1} in the 2θ ranging from 10 to 80°. The calculation formulas of inter-layer spacing (d_{002}) and crystallite height (L_c) based on the XRD spectra are detailed in Additional file 1. The Raman spectroscopy (DXR532) with a wavelength of 532 nm was employed to analyze the defect or disorder information of carbon materials. The surface composition of samples was analyzed through X-ray photoelectron spectroscopy (XPS, Thermo Fisher Nexsa) with a mono-chromicized Al K radiation at 225 W. Nitrogen physisorption measurements were measured at 77 K by Micromeritics ASAP2460 analyzer. The wood-derived carbon materials were degassed at 200 °C for 8 h before the test. The pore size distribution was analyzed from the density functional theory (DFT) model based on the adsorption isotherm. The specific surface area (SSA) was calculated from the Brunauer–Emmett–Teller (BET) method. Single point adsorption total pore volume (V_t) was calculated at the P/P$_0$ of about 0.99.

2.5 Electrochemical measurements
The three-electrode setup was utilized for the electrochemical tests at room temperature ($\sim$ 25 °C) on the CHI 760E electrochemical workstations. In 6 M KOH aqueous electrolyte, the as-prepared wood-derived carbon monoliths were employed as free-standing working electrodes and counter electrode (the mass loading was about 40 mg cm^{-2} and the density was about 500 mg cm^{-3}), nickel foam was used as the collector, the cellulose paper (NKK-MPF30AC-100) was served as the separator, and the Hg/HgO electrodes was functioned as the reference electrodes. Significantly, in 6 M KOH electrolyte, the symmetrical supercapacitors (SSCs) were assembled with FA-OC2//FA-OC2 electrodes. Cyclic voltammetry (CV), galvanostatic charge–discharge (GCD), electrochemical impedance spectroscopy (EIS, from 10^5 to 10^{-2} Hz) and long-term cycling stability were performed. More details about electrochemical measurements and calculation of specific capacitance, energy density, and powder density are stated in Additional file 1.

3 Results and discussion
3.1 Morphology and microstructure characterization
3.1.1 Microscopic morphology of the carbonized samples
Basswood has unique physical properties (anisotropic structure) and chemical compositions (mainly cellulose, hemicellulose, and lignin), and can be functionalized by modifying its structure and/or composition (Chen et al. 2020; Wang et al. 2021c). FA was utilized as the potential precursor to construct N-functionalized carbonaceous material considering the coexistence of amino-groups (–NH_2) and carbonyl groups (C=O) in its structure (Zhang et al. 2021). Figure 1 graphically illustrates the preparation process of N doped O-rich basswood derived carbon monoliths. Briefly, the natural basswood blocks with tracheid structures were cut perpendicularly to its growth direction into thin slices with a thickness of about 0.1 cm (Additional file 1: Fig. S1a, b). FA was the medium of the solvothermal reaction for basswood. The reaction system was kept at 120 °C for 3 h to completely expel the intra-tracheid pressure so as to allow the FA to fully permeate into basswood slices. The high temperature (180 °C) and autogenous hyperbaric environment in the autoclave enhanced the reactivity of formamide. Formamide could form one-dimensional polyformamide chains through the Schiff-base condensation reaction (Yang et al. 2021; Liu et al. 2021; Li et al. 2022). Basswood contained abundant –OH/–COOH groups (Huang et al. 2019a; Chen et al. 2020). The activity of those groups was
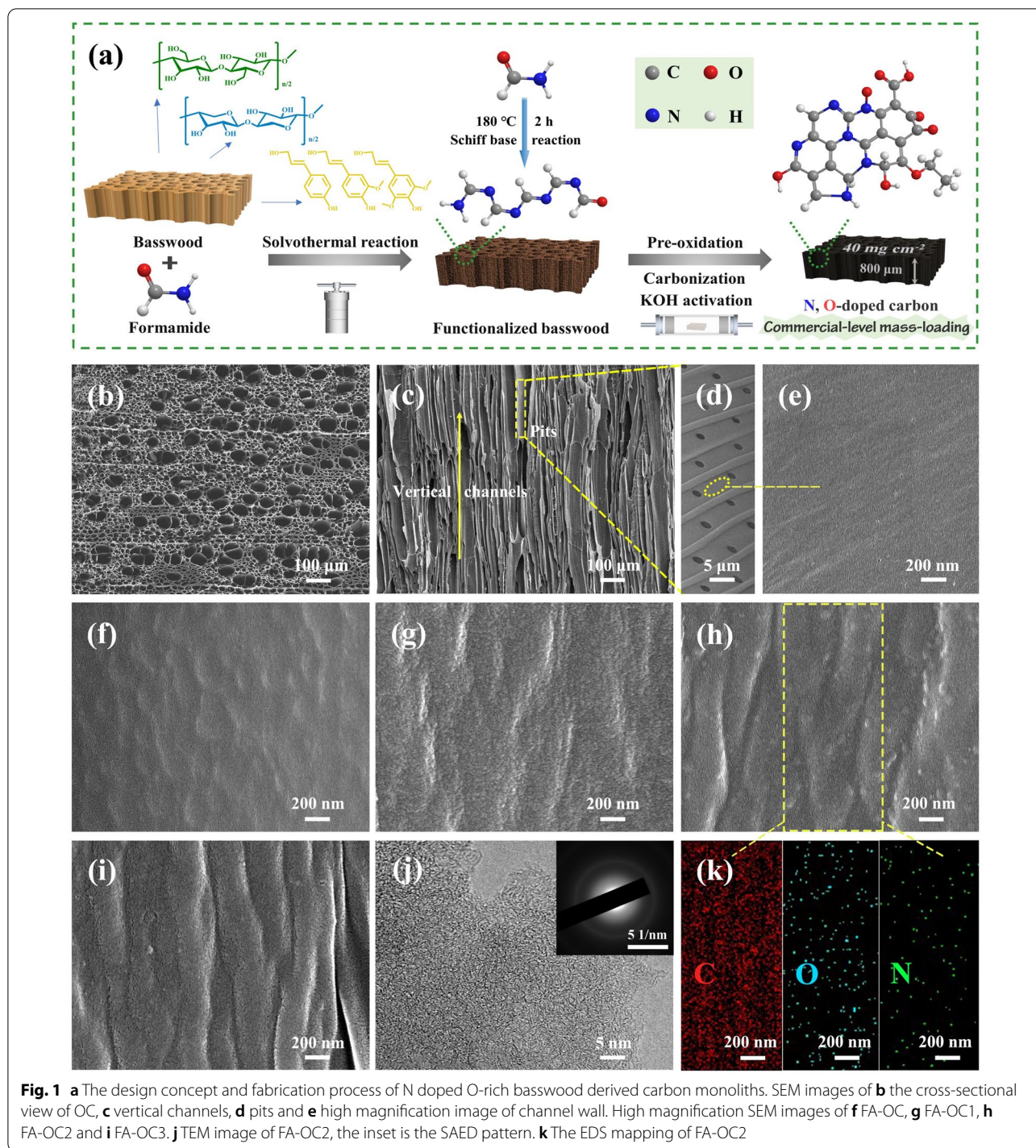
Fig. 1 **a** The design concept and fabrication process of N doped O-rich basswood derived carbon monoliths. SEM images of **b** the cross-sectional view of OC, **c** vertical channels, **d** pits and **e** high magnification image of channel wall. High magnification SEM images of **f** FA-OC, **g** FA-OC1, **h** FA-OC2 and **i** FA-OC3. **j** TEM image of FA-OC2, the inset is the SAED pattern. **k** The EDS mapping of FA-OC2

also enhanced during the solvothermal process (Wang et al. 2020; González-Arias et al. 2021; Lachos-Perez et al. 2022). Hence, formamides or polyformamides (containing –NH₂) can be combined with wood at the molecular level through dehydration condensation (Li et al. 2022).

The FA-OC carbon monoliths were obtained by the subsequent pre-oxidation and carbonization process.

The pore size was further refined by mild KOH activation, which includes chemical activation and physical activation. When the temperature exceeded 400 °C (the melting point of KOH was 360 °C), KOH was

gradually transformed into K_2CO_3, until KOH was completely consumed at about 600 ℃ ($6\ KOH + 2\ C \rightarrow 2\ K + 3\ H_2 + 2\ K_2CO_3$). When the temperature higher than 700 ℃, K_2CO_3 gradually decomposed into K_2O and CO_2 until it disappeared completely at about 800 ℃ ($K_2CO_3 \rightarrow K_2O + CO_2$). Moreover, the intermediates (K_2CO_3, K_2O, and CO_2) can be further reduced by carbothermal reduction at temperatures over 700 ℃ ($K_2CO_3 + 2\ C \rightarrow 2\ K + 3\ CO$, $K_2O + C \rightarrow 2\ K + CO$, $CO_2 + C \rightarrow 2\ CO$), and the generated metallic K intercalated into the carbon lattices to catalyze carbon lattice rearrangement to improve the degree of graphitization or expand the carbon lattice spacing to form nanopores (Wu et al. 2016; Govind Raj and Joy 2017). But the reported methods usually employed a high dosage to achieve full activation effect, and their strong activation inevitably destroyed the integrity of carbon materials and even collapsed the structure (Liu et al. 2020). Other than that, the severe etching sacrificed the content of heteroatom doping (Wabo and Klepel 2021). To maintain the integrity of the self-supporting structure and retain the surface chemical properties of FA-OC, we immersed FA-OC in KOH ethanol solution with relatively low concentration (100 mM, 200 mM and 300 mM, respectively) and then activated them. The final activated products (FA-OC1, FA-OC2 and FA-OC3) exhibited good integrity and only shrank in size (Additional file 1: Fig. S1a, c). The mass loading of as obtained electrodes (~ 40 mg cm^{-2}, ~ 800 μm) was not only higher than most of literature reports (summarize in Additional file 1: Table S9), but also fully meets the requirements of commercial-level supercapacitors (~ 10 mg cm^{-2}).
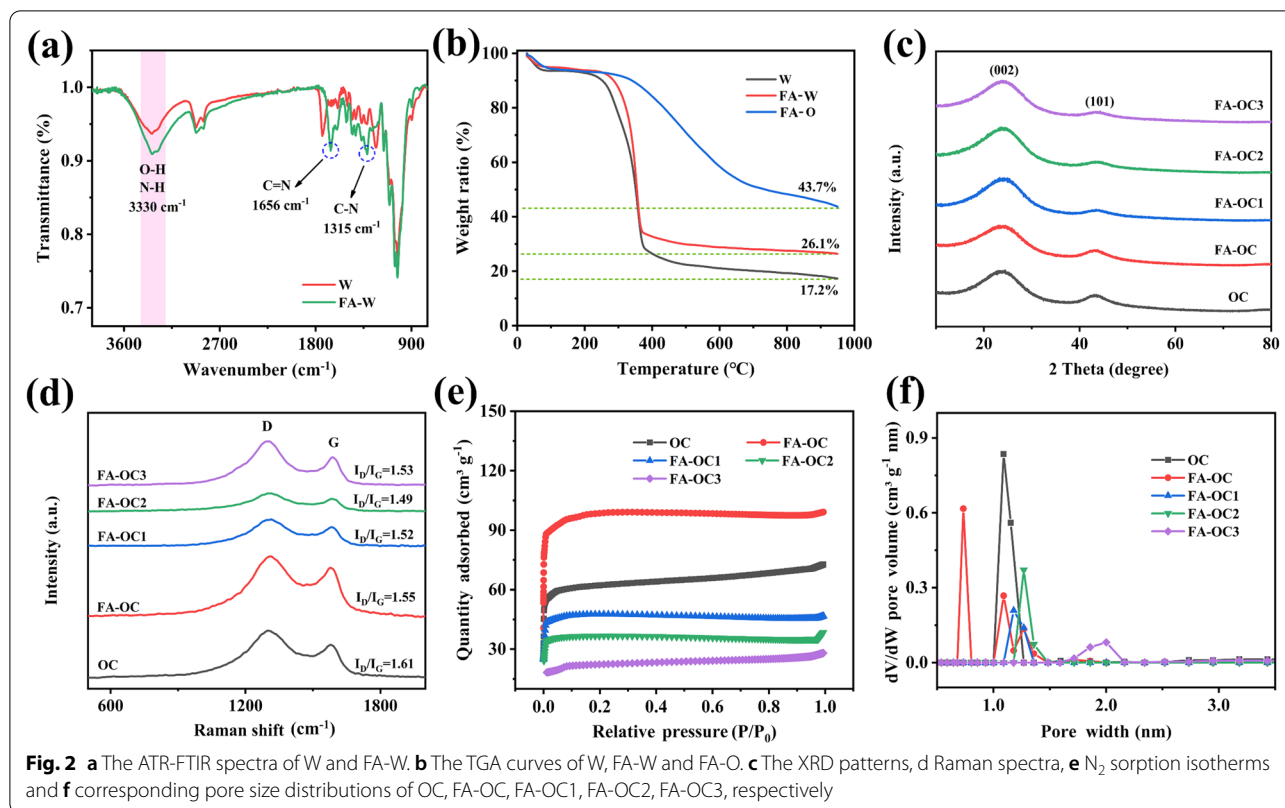
The surface morphologies and microstructures of samples were observed by SEM and HRTEM. As shown in Fig. 1b–e, the OC inherited the vertical and smooth vessel structure of natural wood as the electrolytes buffer cells to shorten the transport distance of electrolyte ions, and a number of pits (Fig. 1d) on the wall provided favorable paths for the rapid transfer of electrolyte ions between the adjacent channels (Wang et al. 2021b, 2021c, 2021d). The self-supporting structure of FA-OC was well maintained and the channel walls became rough (Fig. 1f). The FA-OC samples activated by small dosage of KOH (FA-OC1, FA-OC2 and FA-OC3) retained the original low tortuosity channels (Additional file 1: Fig. S2), and only the vessel walls slightly wrinkled, which was more pronounced with the increase of KOH concentration (Fig. 1g–i). The mild KOH activation strategy maintained the anisotropic structure inherited from the wood chips, and the low-flexibility channels and continuous conductive paths were conducive to the respectable capacitive performance. To confirm the surface chemistry of the activated samples, the elemental mapping images

(Fig. 1k) from EDS test were used to detect the distribution of elements. Clearly, the FA-OC2 was composed of evenly distributed C/N/O elements. Furthermore, the microstructure of FA-OC2 was explored by HRTEM and the corresponding image is shown in Fig. 1j, which exhibited disordered turbostratic structure and few pseudographitic domains. The absence of lattice fringe in the SAED pattern (Fig. 1j inset) also confirmed the amorphous feature of FA-OC2.

3.1.2 Characterization of the samples before carbonization

The grafting of N-containing functional groups on the basswood after the solvothermal process was preliminary confirmed by ATR-FTIR spectra. As shown in Fig. 2a, compared to the W, the absorption peaks at 3330 cm^{-1}, 1650 cm^{-1}, and 1315 cm^{-1} of FA-W indicated the stretching vibration of N–H, C=N, and C–N bonds. In addition, the absorption peaks belonging to the stretching vibration of non-conjugated C=O and C–O functional groups at 1737 cm^{-1} and 1228 cm^{-1} disappeared, demonstrating the wood monoliths were successfully N-functionalized via a convenient solvothermal reaction (Zhang et al. 2021). The natural basswood was light yellow and turn brown after the solvothermal reaction (Additional file 1: Fig. S1a), which was ascribed to the solvothermal carbonation of basswood and pendant amine-groups (Daikopoulos et al. 2014; Wang et al. 2020). The functionalization of precursor by N-containing compounds via solvothermal reaction was a universal strategy, which may be suitable for scaling up.

Furthermore, the superiority of the pre-oxidation was highlighted by TGA curves, and the differences in pyrolysis behavior of the W, FA-W and pre-oxidized FA-W (abbreviated as FA-O) are shown in Fig. 2b. The weight loss of the W before 250 °C was caused by the removal of its inherent free water. With the increase in temperature (250–400 ℃), the rapid weight loss was due to the six-membered ring opening, glycosidic bond breakage and oxygen-containing double bond rearrangement in cellulose and hemicellulose molecules. The shoulder peak at low temperature (~ 250 ℃) belonged to the degradation of hemicellulose, while the peak at high temperature (~ 400 ℃) was recognized as the degradation of cellulose (Peng et al. 2019). Different from cellulose and hemicellulose, the decomposition process of lignin was very slow and complicated due to their native heterogeneous structure, with continuous weight loss from the initial to the end and no peak observed (Leng et al. 2022). The residual amount of W was only 17.2%. In the case of FA-W, the decomposition generally followed similar thermal behaviors as W, but the shoulder peak shifted to the higher temperature (~ 280 ℃). The total yield was calculated as 26.1%, which was higher than that of W, indicating that

Fig. 2 a The ATR-FTIR spectra of W and FA-W. **b** The TGA curves of W, FA-W and FA-O. **c** The XRD patterns, d Raman spectra, **e** N$_2$ sorption isotherms and **f** corresponding pore size distributions of OC, FA-OC, FA-OC1, FA-OC2, FA-OC3, respectively

the FA reacted with the basswood components and promoted its conversion to carbonaceous materials (Liu et al. 2019a). The pre-oxidation was carried out in the air at 260 ℃ for 6 h (FA-O) and the final carbonization yield was increased to 43.7%. Taking the low price of basswood, formamide, and air into consideration, the production cost of FA-OC samples is inexpensive. The mechanism of pre-oxidation process in enhancing the characteristics of wood-derived carbon has been systematically investigated (Shang et al. 2018; Du et al. 2021). In short, the pre-oxidation process removed the physically adsorbed water, bound water and light-volatiles, promoted the intermolecular cross-linking, stabilized the self-supporting structure and improved the pyrolysis residual rate. More importantly, the pre-oxidation increased the O content of wood by converting alkyl groups to peroxides and alcohols, which provided additional pseudo-capacitance and improved the hydrophilicity of electrodes.

3.1.3 Microstructure characterization of the carbonized samples

XRD patterns were collected to further analyze the crystalline nature of the carbonized samples. The characteristic peaks of OC, FA-OC and FA-OC1/FA-OC2/FA-OC3 were all at around 23° (002) and 43° (101) (Fig. 2c). The peak intensity of the broad peak was weak, indicating a low degree of graphitization and crystallization (Zhong et al. 2021; Yu et al. 2022). To further reveal the difference of disordered degree and crystallinity between FA-OC and FA-OC1/FA-OC2/FA-OC3, the interlayer spacing (d_{002}) and crystallite height (L_c) were calculated according to Bragg and Scherrer formulas (Additional file 1: Eqs. S1 and S2)). The d_{002} decreased from 0.378 nm for FA-OC to 0.371 nm for FA-OC2, demonstrating that the interlayer spacing was shrunk and tended to generate partially pseudographitic domains (nano-graphite clusters), which might be due to the intercalation of a small amount of metallic K into the carbon lattice to catalyze graphitization during the activation process (Govind Raj and Joy 2017; Xia et al. 2018). However, with the increase of the concentration of KOH, more metallic K incorporated into the carbon lattice resulted in extended d_{002} of FA-OC3 (0.373 nm). Clearly, the interlayer spacing of the samples (before and after KOH activation) was much larger than that of graphite (0.334 nm), indicating their typical disordered structure. On the other hand, the L_c of FA-OC and FA-OC1/FA-OC2/FA-OC3 was 1.0244, 1.1211, 1.1294 and 1.1034 nm, respectively. The L_c of the activated samples was larger than that of FA-OC. The L_c of the activated samples increased at first and then decreased, which indicated that KOH can catalyze the formation of ordered nano-graphite clusters

and the catalytic effect was related to the dosage. These results were consistent with the phenomenon observed from HRTEM image (Fig. 1j) that disordered carbon matrix accompanied by a small amount of short-range pseudographitic structure. The pseudographitic structure enhances the conductivity of the carbon skeleton and facilitates the migration and transfer of electrons, thus ensuring the decent rate performance of electrodes, especially at high current densities.

Raman spectra (Fig. 2d) were used to further analyze the defect or disorder information of carbon materials. All samples exhibited evident peaks at ~ 1340 cm^{-1} and ~ 1590 cm^{-1}, which represented D-band (amorphous sp^3 carbon) and G-band (ascribed to the graphitic sp^2 carbon), respectively. Typically, the relative peak intensity ratios of D and G bands (I_D/I_G) were utilized to assess the disorder degree of carbon materials (Jjagwe et al. 2021; Chen et al. 2022). The pre-oxidation suppressed the graphitization of the carbon materials (Du et al. 2021). The graphite layers of the pre-oxidized samples tended to bend and entangle randomly during the subsequent carbonization process rather than grow and rearrange, thus forming a large interlayer spacing (Lin et al. 2020), and the I_D/I_G of OC and FA-OC was as high as 1.61 and 1.55, respectively. In the KOH activation process, a small amount of metallic K could intercalate into the carbon lattice to catalyze the formation of nano-graphite clusters (Govind Raj and Joy 2017; Xia et al. 2018), but excessive metallic K would expand the interlayer spacing and disrupt the arrangement of the ordered graphite clusters. Consequently, the I_D/I_G decreased from 1.55 for FA-OC to 1.49 for FA-OC2, but increased to 1.53 for FA-OC3 with the further increase of KOH concentration. The I_D/I_G of all the samples was greater than 1, which indicated abundant defects and disordered structure (Wang et al. 2022b). The results of Raman spectra were consistent with those of the HRTEM image and XRD patterns.
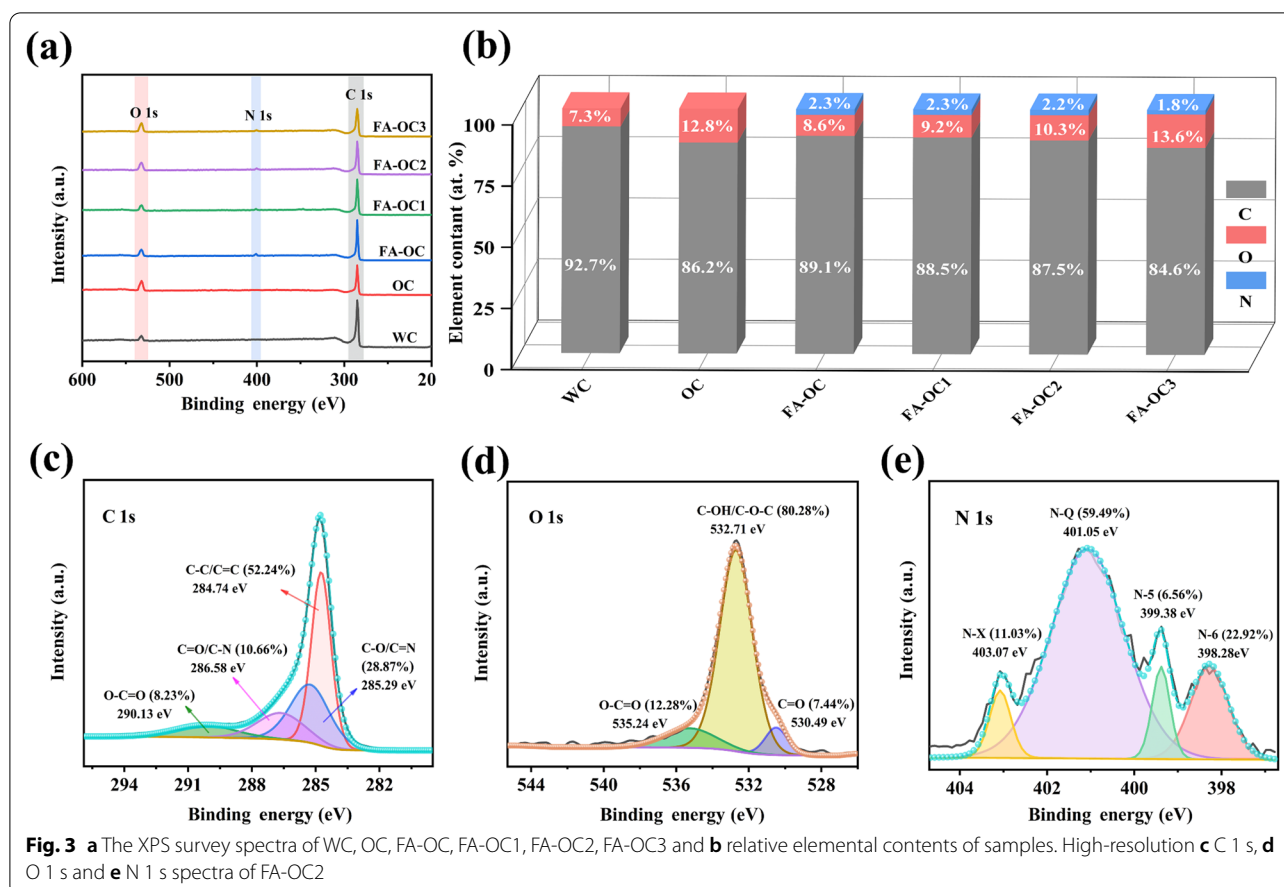
The pore evolutions were analyzed by N$_2$ sorption isotherms and pore size distribution profiles (Fig. 2e, f). All the samples exhibited an increase in the amount of adsorbed N$_2$ at low-pressure region ($P/P_0 < 0.1$) and a convex trail at high-pressure region ($P/P_0 > 0.9$), which were belonged to the micro/macro-porous character according to IUPAC classification (Thommes et al. 2015; Chen et al. 2021a). The pre-oxidation process enhanced the cross-linking degree of basswood components and inhibited the violent decomposition during pyrolysis, hence the SSA (204.83 m^2 g^{-1}) and V$_t$ (0.13 cm^3 g^{-1}) of OC were both slightly higher than those of WC reported in the literature (Tang et al. 2018). The intermolecular reactions between FA and basswood components produced a number of ultra-micropores (~ 0.6 nm) and increased the SSA of FA-OC to 312.73 m^2 g^{-1} (Additional

file 1: Table S1). Ultra-micropores significantly increase the specific capacitance through desolvation of electrolyte ions at low current densities, but electrolyte ions do not have enough time to desolvate at high current densities, resulting in seriously decay of capacitance (Ding et al. 2020). After KOH activation, the ultra-micropores of the FA-OC were widened to large micropores and the pore size gradually became larger with the increase of KOH concentration, and the pore sizes of FA-OC1, FA-OC2 and FA-OC3 were concentrated at 1.2 nm, 1.3 nm and 2.0 nm, respectively. The large micropores ensured high specific capacitance at low current density and improved ion accessibility at high current density.

3.1.4 Surface functional group analysis of the carbonized samples

XPS analysis was conducted to get more insights into the changes in the surface functional groups of samples. The survey spectra for all samples are exhibited in Fig. 3a, with prominent peaks centered at 284.8, 532.7 and 400.3 eV designated as C 1 s, O 1 s and N 1 s, respectively (Ran et al. 2021; Teng et al. 2021; Zheng et al. 2021b). The quantitative analysis results are summarized in Fig. 3b and Additional file 1: Table S1. Compared with WC (7.3 at.%), the increased intensity of O 1 s peak in OC (12.8 at.%) confirmed that the pre-oxidation process introduced more O-containing functional groups. Comparing FA-OC with OC (Fig. 3a, Additional file 1: Fig. S3), the emerging N 1 s peak in FA-OC (2.3 at.%) proved that the FA solvothermal process successfully introduced N-containing functional groups into basswood, which was consistent with the results of ATR-FTIR spectra. In addition, the absence of N 1 s peaks in OC indicated that the inert N$_2$ molecules did not react with carbon matrix during the carbonization process. Hence, the N in FA-OC should be entirely derived from grafted N-containing groups formed in the solvothermal process (Lu et al. 2020). Encouragingly, even at such high carbonization temperature (1000 ℃), the N-doping content was comparable or higher than other N-doped carbon materials (Oh et al. 2019; Kim et al. 2019; Guo et al. 2020; Thongsai et al. 2021). Furthermore, the increased O 1 s content of FA-OC1, FA-OC2 and FA-OC3 was ascribed to the hydroxide reduction and carbon oxidation initiated by KOH activation (Lü et al. 2022). Notably, the N 1 s content of FA-OC1 (2.3 at.%) and FA-OC2 (2.2 at.%) was almost the same as that of FA-OC (2.3 at.%), but that of FA-OC3 decreased (1.8 at.%), which indicated that excessive intercalation of metallic potassium lead to partly collapse of the N-containing carbon monolith (Liu et al. 2020).

Detailed analysis of FA-OC2 was performed by core level fitting. As shown in Fig. 3c, four individual

Fig. 3 a The XPS survey spectra of WC, OC, FA-OC, FA-OC1, FA-OC2, FA-OC3 and **b** relative elemental contents of samples. High-resolution **c** C 1 s, **d** O 1 s and **e** N 1 s spectra of FA-OC2

component peaks were extracted from the high-resolution C 1 s spectrum with binding energies of 284.7, 285.3, 286.6 and 290.1 eV, corresponding to the C–C/C=C, C–O/C=N, C=O/C–N, and O–C=O, respectively (Xu et al. 2021; Zhao et al. 2022). The high-resolution O 1 s spectrum exhibited in Fig. 3d demonstrated the co-existence of multiple oxygen-based groups covering quinone groups (C=O, 530.5 eV), phenol/ether groups (C–OH/C–O–C, 532.7 eV) and carboxylic groups (O–C=O, 535.2 eV) (Hou et al. 2021). The high-resolution N 1 s spectrum was deconvoluted into four individual peaks at 398.3, 399.4, 401.1 and 403.1 eV, respectively (Fig. 3e), which corresponded to pyridinic N (N-6, 22.9%), pyrrolic/pyridone N (N-5, 6.6%), quaternary N (N-Q, 59.5%) and N-oxide (N-X, 11.0%), respectively (Liu et al. 2022a). During the carbonization process, N-6 was preferentially formed, but with the increase of temperature, the thermally unstable N-6 and N-5 tended to be transformed into thermally stable N-Q (Zhang et al. 2015). The N-6 and N-Q accounted for 80% of the total N. Normally, the pseudo-capacitive was triggered on O-surface groups (carbonyl/hydroxyl/carboxyl) and negatively charged N-6/N-5 (Additional file 1: Fig. S4). The co-existence of

N/O-containing functional groups not only contributed to the pseudo-capacitance but also the hydrophilicity. Besides, the positively charged N-Q enhanced the electron transfer kinetics at the electrode/electrolyte interface, and heightened the conductivity of the electrodes (Ghosh et al. 2020).

3.2 Electrochemical performance

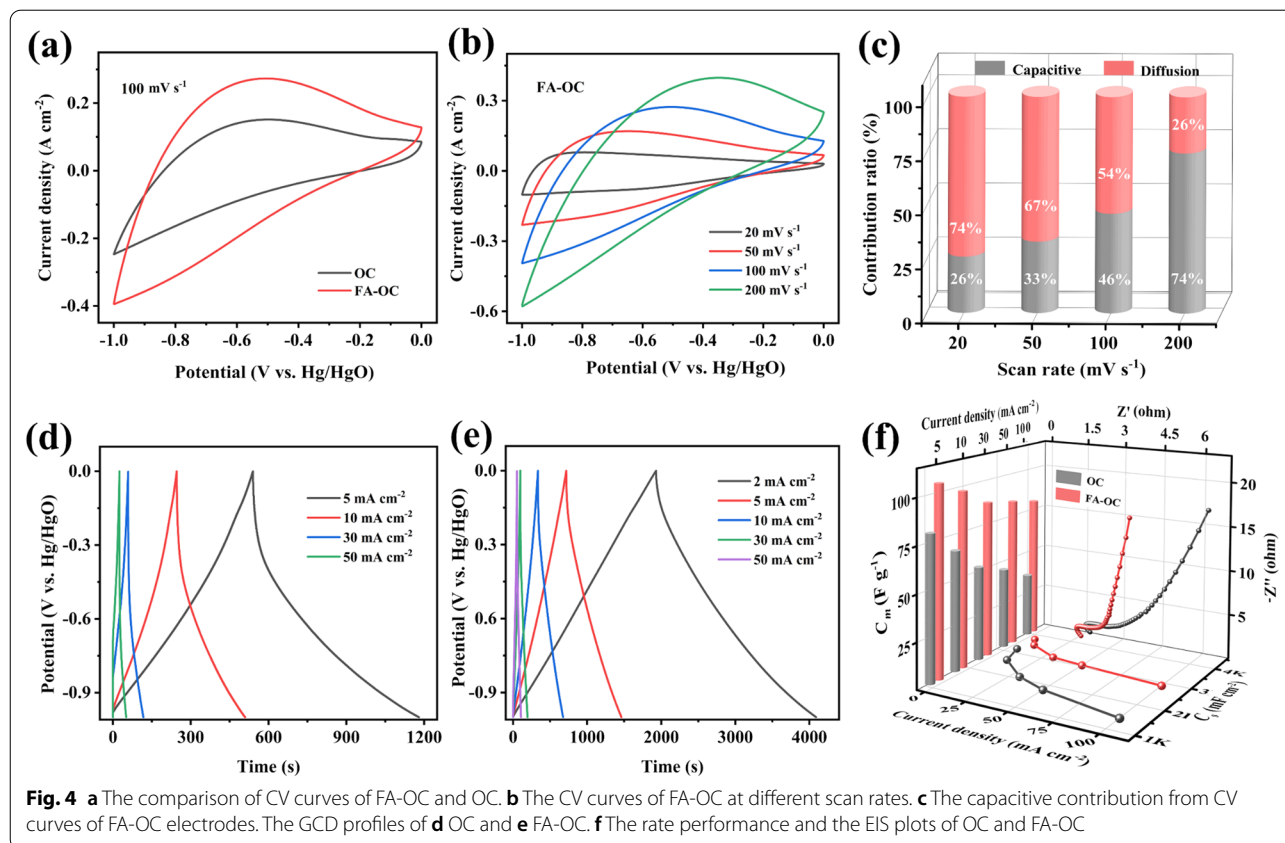### 3.2.1 Electrochemical performance in three-electrode system

To demonstrate the pore structure, heteroatom doping and self-supporting structure for improving electrochemical properties, the electrochemical behaviors of the samples were evaluated through the three-electrode system in 6M KOH electrolyte. Both the WC and OC exhibited hepar-like CV profiles (Additional file 1: Fig. S5a), which might be caused by their undeveloped pore structure. The GCD curve of WC was extremely distorted at 10 mA cm^{-2} (0.19 A g^{-1}), and the specific capacitance was low (C_s of 881.2 mF cm^{-2}, C_m of 25.5 F g^{-1}, Additional file 1: Fig. S5b). The finite capacitance of WC was in accordance with the other literatures (Tang et al. 2018; Ma et al. 2020). Whereas for OC electrodes, the obvious

faradaic hump indicated the pre-oxidation was beneficial to enhance the capacitance performance, and the specific capacitance was elevated to 2640.0 mF cm^{-2} (66.0 F g^{-1}) at 10 mA cm^{-2} (0.17 A g^{-1}).

Compared with OC, although the CV curve of FA-OC still kept hepar shape, its enclosed area was almost doubled at 100 mV s^{-1}, and the pseudo-capacitance hump was more obvious (Fig. 4a). To further comprehend the relationship between electrochemical behavior and heteroatom doping, CV measurements of FA-OC with different scan rates (from 20 to 200 mV s^{-1}) were carried out and are exhibited in Fig. 4b. The capacitive/diffusion-controlled contributions were calculated from CV curves by the Duun's method (Augustyn et al. 2014) (Additional file 1: Eqs. S3–S5) and are summarized in Fig. 4c. The pseudo-capacitive contribution of FA-OC electrodes upped to 74% at 20 mV s^{-1} and still remained 26% at 200 mV s^{-1} (Additional file 1: Fig. S6a–d). The high contribution of pseudo-capacitance was associated with N/O-containing functional groups. In addition, as the scan rate increased, the CV curves were gradually deformed due to the slow redox kinetics of heteroatom-containing functional groups and the solvated electrolyte ions did not have enough time to desolvate and enter the ultra-micropores. The advancement of capacitance

performance of FA-OC compared with OC was quantified based on Additional file 1: Eqs. S6–S8 via GCD profiles at different current densities (Fig. 4d, e) to reflect the role of ultra-micropores and N/O-containing functional groups. As presented in Fig. 4f and Additional file 1: Tables S2, S3, the calculated specific capacitance of OC was 3190.0 mF cm^{-2} at 5 mA cm^{-2} (0.09 A g^{-1}) and decreased to 1431.6 mF cm^{-2} at 100 mA cm^{-2} (1.85 A g^{-1}), and the corresponding C_m and C_v reduced from 79.8 F g^{-1} and 39.9 F cm^{-3} to 35.8 F g^{-1} and 17.9 F cm^{-3}, while the C_s of FA-OC was 4346.1, 3775.0, 2759.2 mF cm^{-2} at 2, 5, 100 mA cm^{-2} (0.04, 0.10, 2.00 A g^{-1}), respectively (C_m of 120.7, 104.9 and 79.9 F g^{-1}, C_v of 54.3, 47.2 and 34.5 F cm^{-3}). Compared with OC, the increased capacitance of FA-OC at low current densities was due to the combined effects of desolvation of ions in ultra-micropores and greater O doping ratio along with additional N doping, while the improved capacitance retention at high current density was benefited from the improvement of N-Q and N-X species on the conductivity of the carbon matrix.

The Nyquist plots are also presented in Fig. 4f to investigate the change of resistance, and the fitted EIS plots and corresponding equivalent circuit models are exhibited in Additional file 1: Fig. S6e. The X-axis intercept (R$_s$)

Fig. 4 **a** The comparison of CV curves of FA-OC and OC. **b** The CV curves of FA-OC at different scan rates. **c** The capacitive contribution from CV curves of FA-OC electrodes. The GCD profiles of **d** OC and **e** FA-OC. **f** The rate performance and the EIS plots of OC and FA-OC
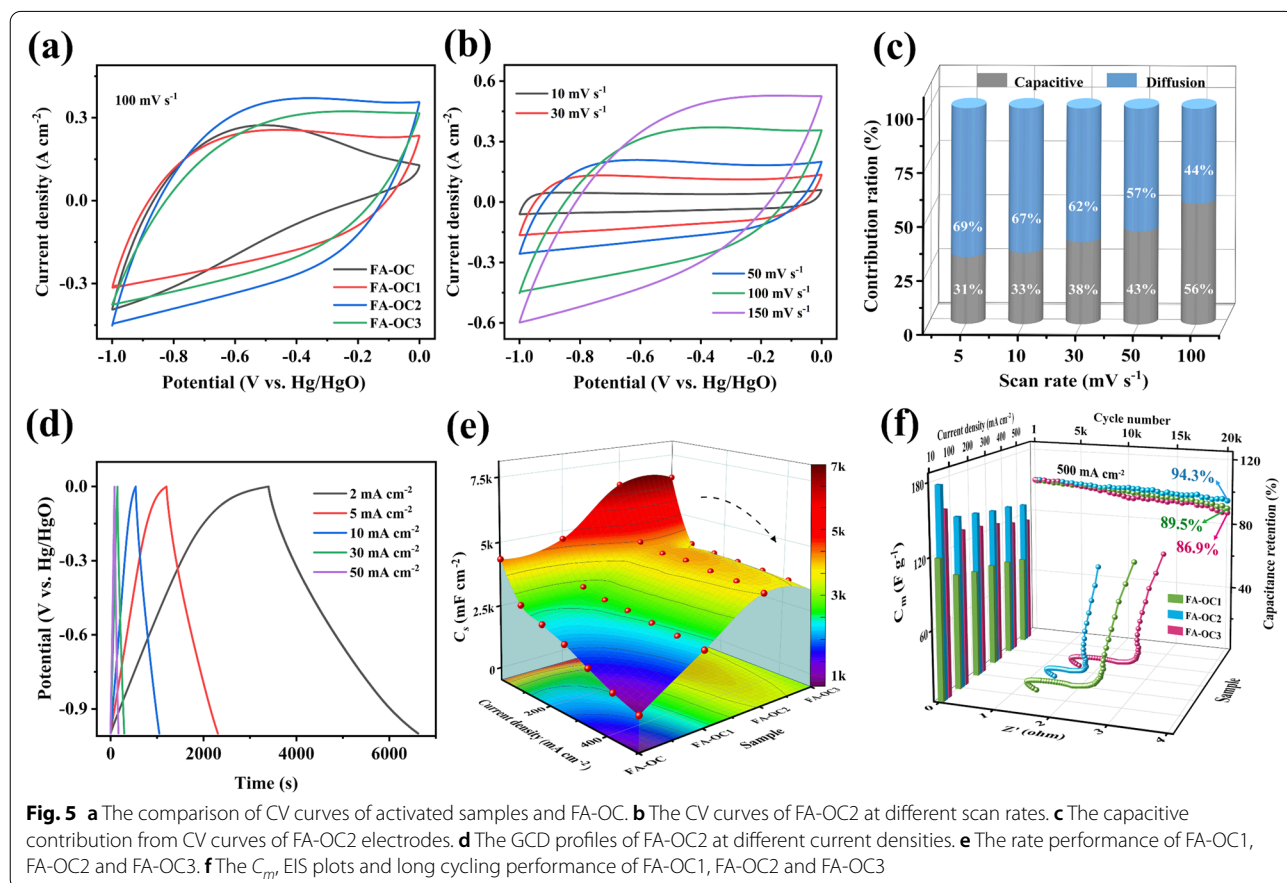
for OC and FA-OC was both nearly 1 Ω, which meant the small internal resistance assigned by high-temperature carbonization. In the high-frequency region, the R_{ct} related to the charge transfer resistance of FA-OC was smaller than OC. In the low-frequency region, the slope of fitted EIS curves of FA-OC was steeper than that of the OC (Additional file 1: Table S4), indicating their smaller diffusion resistance, higher electrical conductivity, and faster ion diffusion rate, which was responsible for the improved rate capability.

Although the rate capability of FA-OC was improved compared to OC, the enhancement was still unsatisfactory. For FA-OC, due to the ion-sieving effects (Eliad et al. 2001), few electrolyte ions can enter the interior of ultra-micropores (~0.6 nm) especially at high current density. The rapid loss of capacitance at high current density was mainly caused by the poor ionic accessibility and limited oxidation–reduction reaction kinetics of N/O-containing functional groups (Ding et al. 2019). The specific capacitance was only 821.8 mF cm^{-2} (23.1 F g^{-1}, 10.3 F cm^{-3}) at 500 mA cm^{-2} (9.62 A g^{-1}). To further improve their comprehensive capacitance performance, the mild KOH activation method was adopted. The micropores were widened to reduce the influence of ion

sieving and provide more electric double-layer capacitance. On the other hand, the low KOH concentration introduced more O-containing species to elevate pseudo-capacitance contribution without losing the N-containing functional groups through mild hydroxide reduction and carbon oxidation.

The capacitance performances of the activated samples (FA-OC1, FA-OC2 and FA-OC3) were tested and the results are depicted in Fig. 5. The CV curves of all the activated electrodes presented the rectangular shape and covered larger enclosed area than FA-OC (Fig. 5a), indicating that the activated samples possessed higher charge storage capability. In detail, the FA-OC2 maintained the rectangular shape even at the scan rate of 100 mV s^{-1} (Fig. 5b), demonstrating its ameliorated rate capability. Moreover, the pores of the heteroatom-rich FA-OC2 electrode are dominated by large micropores. As the scan rate increased, the CV curve gradually turned to shuttle-shape due to the increased ion transport resistance and the delayed Faradaic reaction. There is no linear relationship between the specific surface area and capacitance because not all micropores are electrolyte ions accessible (Yan et al. 2014). Although the SSA of FA-OC2 was smaller than that of FA-OC1, the micropores of

Fig. 5 **a** The comparison of CV curves of activated samples and FA-OC. **b** The CV curves of FA-OC2 at different scan rates. **c** The capacitive contribution from CV curves of FA-OC2 electrodes. **d** The GCD profiles of FA-OC2 at different current densities. **e** The rate performance of FA-OC1, FA-OC2 and FA-OC3. **f** The C_m, EIS plots and long cycling performance of FA-OC1, FA-OC2 and FA-OC3

the former were wider, which greatly weakened the hindrance of ion sieving effect on the electric double-layer capacitance and provided more active sites for energy storage. Additionally, in aqueous electrolyte (6M KOH), the capacitive performance depended more on heteroatom-containing functional groups than on specific surface area (Wei and Yushin 2012). Although the N-doping content of FA-OC2 was almost identical to that of FA-OC1, the O-doping content of FA-OC2 was higher than that of FA-OC1. Thus, the superior capacitive performance of FA-OC2 was reasonable. With the increase of KOH concentration, the small micropores were gradually expanded into large micropores, and the content of O-containing functional groups was improved. However, excessive KOH sacrificed part of the N content due to the strong etching reaction, resulting in the decrease of capacitive performance for FA-OC3.

At the scan rate of 100 mV s^{-1}, the contribution of electric double-layer capacitance for FA-OC, FA-OC1, FA-OC2 and FA-OC3 was 46%, 61%, 56% and 51%, respectively (Fig. 5c, Additional file 1: Figs. S6–S9), indicating that KOH activation improved the utilization of micropores and thus increased the double-layer capacitance. Besides, the introduction of O-containing functional groups during KOH activation process provided additional pseudo-capacitance. At the current density of 2 mA cm^{-2} ($\sim$0.05 A g^{-1}), the specific capacitance (C_s, C_m, C_v) of the FA-OC1, FA-OC2 and FA-OC3 was 4688.5 mF cm^{-2} (154.5 F g^{-1}, 58.6 F cm^{-3}), 6538.5 mF cm^{-2} (223.9 F g^{-1}, 81.7 F cm^{-3}) and 6516.3 mF cm^{-2} (229.4 F g^{-1}, 81.5 F cm^{-3}), respectively (Fig. 5d, e). Upon increasing the current density up to 100 mA cm^{-2} (2.27 A g^{-1} for FA-OC1, 2.50 A g^{-1} for FA-OC2, 2.63 A g^{-1} for FA-OC3), the specific capacitance (C_s, C_m, C_v) of FA-OC1, FA-OC2 and FA-OC3 retained 2973.1 mF cm^{-2} (97.8 F g^{-1}, 37.2 F cm^{-3}), 4259.4 mF cm^{-2} (145.9 F g^{-1}, 53.2 F cm^{-3}) and 3763.4 mF cm^{-2} (133.2 F g^{-1}, 47.0 F cm^{-3}), respectively (Fig. 5f, Additional file 1: Table S5-S7). The inferior performance of FA-OC1 to FA-OC2 was due to insufficient KOH dosage and low effective specific surface area. However, FA-OC3 exhibited a slightly lower capacitance than FA-OC2 as the current density increased, which was due to the excessive activation of KOH leading to the loss of some N/O species. Thus, the appropriate KOH concentration kept a balance between surface-controlled electrical double-layer capacitance and diffusion-controlled faraday pseudo-capacitance, which closed the gap between the initial capacitance and rate performance. The rich N/O functional groups were favorable for the infiltration of electrolyte. The mild activation method maintained vertical channels and stable self-supporting structure, which was conducive to the rapid transport of electrolyte ions and electrons. On the other hand, the micropores matching the electrolyte ion size ensured the accessibility of electrolyte ions at high current density. Even when the current density increased to 500 mA cm^{-2} (12.50 A g^{-1}), the specific capacitance of FA-OC2 remained at 3821.2 mF cm^{-2} (130.9 F g^{-1}, 47.8 F cm^{-3}). This rate performance was far superior to that of some wood-based electrodes and other biomass-based self-supporting electrodes, C_s such as the CCF-SP electrode where the maximum current density applied only reached at 10 mA cm^{-2} (Sun et al., 2021) and the WC@Ag-20@NiCo$_2$S$_4$-20 (Wang et al., 2021d) and WC-E-100-48 (Wang et al., 2021c) electrodes where the C_s decayed by 50% when the current density increased from 1 to 50 mA cm^{-2}.

The volumetric capacitance performance is an essential indicator for portable electronics with limited space. Regrettably, for most supercapacitors, especially those based on powder electrodes, the relationship between volumetric and gravimetric capacitances is contradictory. Generally, the effective surface area available for electrolyte ions of the dense electrodes was limited, and the transport channels of electrolyte ions were tortuous, resulting in poor gravimetric capacitance. While the carbon electrodes with large effective surface area (low density) lost volume capacitance when achieving high gravimetric capacitance. The FA-OC2 electrode benefited from the low tortuosity self-supporting macrostructure and dense microstructure (the mass loading of ca. 40 mg cm^{-2}) as well as abundant heteroatom functional groups. The C_m was 223.9 F g^{-1} at 2 mA cm^{-2} (0.05 A g^{-1}), and the corresponding C_v was 81.7 F cm^{-3}. Compared those values with the results reported in several references, FA-OC2 electrodes showed advantages to some wood-based carbon monoliths and other biomass-derived self-supporting (thick) electrodes. For example, although the cotton rose wood derived carbon monoliths exhibited the C_m of 140 F g^{-1}, the C_v only achieved 28 F cm^{-3} (Ma et al. 2020). The C_m and C_v of the thick electrode derived from delignified basswood (Wang et al. 2021e) was 65 F g^{-1} and 2.67 F cm^{-3}, respectively. The highly dense graphene exhibited a high C_v of 155 F cm^{-3}, and their C_m was only 136 F g^{-1} (Han et al. 2018).

The limited installation space of components in portable electronic devices also requires the maximization of capacitance per unit surface area (termed SSA-normalized capacitance and is computed from Additional file 1: Eq. S9). The inherent capacitive properties can be revealed by the SSA-normalized capacitance. In the literature, some electrodes exhibited high SSA but low SSA-normalized capacitance, such as P-doped thick carbon electrode (959 m^2 g^{-1}, 21.5 μF cm^{-2}) (Wang et al. 2021b),

enzymolysis-treated wood (1418 m^2 g^{-1}, 23.1 µF cm^{-2}) (Wang et al. 2021c), activated fir wood (703.5 m^2 g^{-1}, 40.6 µF cm^{-2}) (Zhang et al. 2019a), petroleum coke derived PCs (2140 m^2 g^{-1}, 12.2 µF cm^{-2}) (Zuliani et al. 2018), and RGO/CFs (525 m^2 g^{-1}, 30 µF cm^{-2}) (Sun et al. 2019), which indicated their insufficient SSA utilization. For FA-OC2 monoliths, the concentrated pore size distribution matching the electrolyte ion size improved the utilization of SSA, and the abundant N/O functional groups provided huge faraday pseudo-capacitance, and the low SSA (126.2 m^2 g^{-1}) corresponded to an ultrahigh SSA-normalized capacitance (177.4 µF cm^{-2}). In particular, the N-6/N-5/−C=O/−OH groups in carbon monoliths were considered to play key roles in enhancing the SSA-normalized capacitance via faradaic redox reaction.

Moreover, the EIS measurements were also performed to investigate the kinetics of the electrodes (Fig. 5f) and the corresponding equivalent electric circuit is exhibited in Additional file 1: Fig. S10. For traditional coated electrodes, there is a lack of continuous conductive channels between active materials, and the additional binders increase the electron transfer resistance. In addition, the intricate microscopic morphology between the active materials results in tortuous electron/electrolyte ion transfer paths and lengthened transfer distance. For the self-supporting FA-OC2 carbon monoliths, the continuous conductive carbon skeleton provides effective paths for electron transfer, and the N-X/N-Q groups enhance the electron transfer kinetics at the electrode/electrolyte interface. The FA-OC2 showed a steeper line at the low-frequency region and a smaller semicircle at the middle-frequency region, and the W$_o$ and R$_{ct}$ were 1.80 Ω and 0.37 Ω, respectively (Additional file 1: Table S8), manifesting their faster electrolyte ion diffusion and transfer rate. The charge transfer resistance was comparable to other wood-based electrodes [CW-P-9.24, 0.78 Ω (Wang et al. 2021b); WC-E-100-48, 0.99 Ω (Wang et al. 2021c)], and distinctly smaller than some of the commercial thick electrodes (NCPC, 20.0 Ω (Lin et al. 2021); LFMP nano-plates, 14.1 Ω (Zhao et al. 2019)) reported in the literature. Furthermore, long-term stability is another vital parameter for evaluating the capacitance performance of electrode materials. We investigated the durability of the FA-OC1/2/3 by cycling between − 1 and 0 V for 20,000 cycles at the current density of 500 mA cm^{-2} (11.36 A g^{-1} for FA-OC1, 12.50 for FA-OC2, and 13.16 for FA-CO3). Notably, FA-OC2 described the ultra-long cycling stability of nearly 94.3% capacitive retention (Fig. 5f).
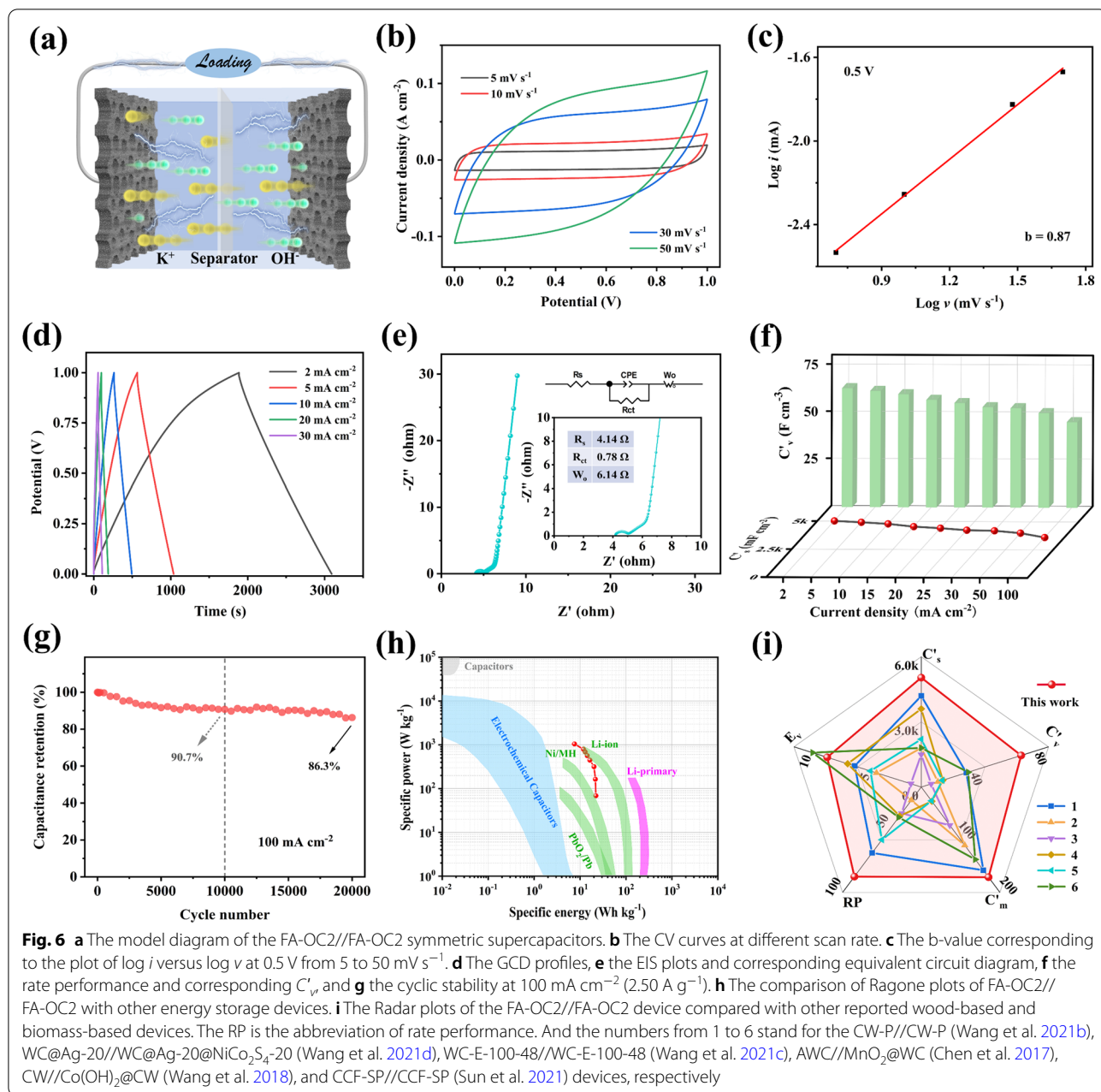
3.2.2 Electrochemical performance in two-electrode system

To further explore the practical performance of FA-OC2, the symmetric supercapacitors (FA-OC2//FA-OC2) were assembled and measured in 6M KOH electrolyte and the

model diagram is exhibited in Fig. 6a. Clearly, the CV curves maintained quasi-rectangular shape at the range from 5 to 50 mV s^{-1} (Fig. 6b), and the corresponding fitted *b* value confirmed the synergistic effect of double-layer capacitance and pseudo-capacitance (Fig. 6c). The GCD curves exhibited the symmetric triangle shape at different current densities (Fig. 6d), implying its superior electrochemical reversibility. Notably, the symmetric two-electrode devices possessed a diminished specific capacitance calculated from GCD curves by Additional file 1: Eqs. S10–S12, which was approximately 80% of that in the three-electrode configuration. Such decrease was probably caused by the increased device resistance and ion transportation resistance (Fig. 6e). The devices presented the C'_s of 5037.5, 4421.3 and 3622.9 mF cm^{-2} at 2, 20 and 100 mA cm^{-2} (0.05, 0.50 and 2.50 A g^{-1}), which corresponded to the C'_m of 172.5, 151.5 and 124.1 F g^{-1}, the C'_v of 63.0, 55.3 and 45.3 F cm^{-3}, respectively (Fig. 6f and Additional file 1: Table S9). In addition, after 10,000 and 20,000 GCD cycles at 100 mA cm^{-2} (2.50 A g^{-1}), the capacitance of FA-OC//FA-OC remained at 90.7% and 86.3%, respectively (Fig. 6g). The energy density and power density are crucial parameters for SCs toward practical applications (quantified based on Additional file 1: Eqs. S13–S18). As illustrated in Ragone plots (Fig. 6h), compared with other energy storage devices, such as electrochemical capacitors, lead batteries (PbO$_2$/Pb), nickel-metal hydride batteries (Ni/MH), primary and secondary lithium-ion batteries (Li primary and Li-ion batteries), the binder-free SSCs assembled with FA-OC2 delivered decent energy density and power density, which filled the gap between traditional capacitors and Li-ion batteries. At the current density of 2 mA cm^{-2} (0.05 A g^{-1}), the maximum energy density achieved 0.65 mWh cm^{-2}, 22.44 Wh kg^{-1}, and 8.15 mWh cm^{-3}, respectively. In addition, the maximum power density obtained at 100 mA cm^{-2} (2.50 A g^{-1}) was 58.0 mW cm^{-2} (1996.4 W kg^{-1} and 725.0 mW cm^{-3}). The initial capacitance, rate capability and energy/power density of the proposed FA-OC2//FA-OC2 devices were comparable or higher than other wood-based and biomass-based devices reported in literature [such as CW-P//CW-P (Wang et al. 2021b), WC@Ag-20//WC@Ag-20@NiCo$_2$S$_4$-20 (Wang et al. 2021d), WC-E-100-48//WC-E-100-48 (Wang et al. 2021c), AWC//MnO$_2$@WC (Chen et al. 2017), CW//Co(OH)$_2$@CW (Wang et al. 2018), and CCF-SP//CCF-SP (Sun et al. 2021)], and the comparison data are visualized in Fig. 6i and Additional file 1: Table S11.

3.2.3 Demonstration of practical application

As illustrated in Fig. 7a, although the mass loading of as-prepared dense thick electrodes was as high as about

Fig. 6 a The model diagram of the FA-OC2//FA-OC2 symmetric supercapacitors. **b** The CV curves at different scan rate. **c** The b-value corresponding to the plot of log *i* versus log *v* at 0.5 V from 5 to 50 mV s^{-1}. **d** The GCD profiles, **e** the EIS plots and corresponding equivalent circuit diagram, **f** the rate performance and corresponding C'_v, and **g** the cyclic stability at 100 mA cm^{-2} (2.50 A g^{-1}). **h** The comparison of Ragone plots of FA-OC2//FA-OC2 with other energy storage devices. **i** The Radar plots of the FA-OC2//FA-OC2 device compared with other reported wood-based and biomass-based devices. The RP is the abbreviation of rate performance. And the numbers from 1 to 6 stand for the CW-P//CW-P (Wang et al. 2021b), WC@Ag-20//WC@Ag-20@NiCo$_2$S$_4$-20 (Wang et al. 2021d), WC-E-100-48//WC-E-100-48 (Wang et al. 2021c), AWC//MnO$_2$@WC (Chen et al. 2017), CW//Co(OH)$_2$@CW (Wang et al. 2018), and CCF-SP//CCF-SP (Sun et al. 2021) devices, respectively

40 mg cm^{-2}, their vertical channels not only acted as buffer cells for the electrolyte to shorten its diffusion distance, but also provided fast channels for transporting electrolyte ions along the thickness direction, and the pits on the walls facilitated the transfer of the electrolyte between the adjacent channels, and the micropores matching the electrolyte ion ensured the effective utilization of the electrolyte ions. On the other hand, these integral self-supporting electrodes with continuous conductive skeleton avoided the excessive interfacial resistance and thus provided the effective paths for electron transfer, and the N-doping enhanced the electron transfer kinetics at the electrode/electrolyte interface. The abundant N/O-functional groups in the carbon matrix not only contributed to the additional pseudo-capacitance but also increased the hydrophilicity of electrodes to facilitate the rapid diffusion of electrolyte ions. Although the N/O-containing functional groups provided additional pseudo-capacitance, they were not directly participated in the conversion reaction, implying
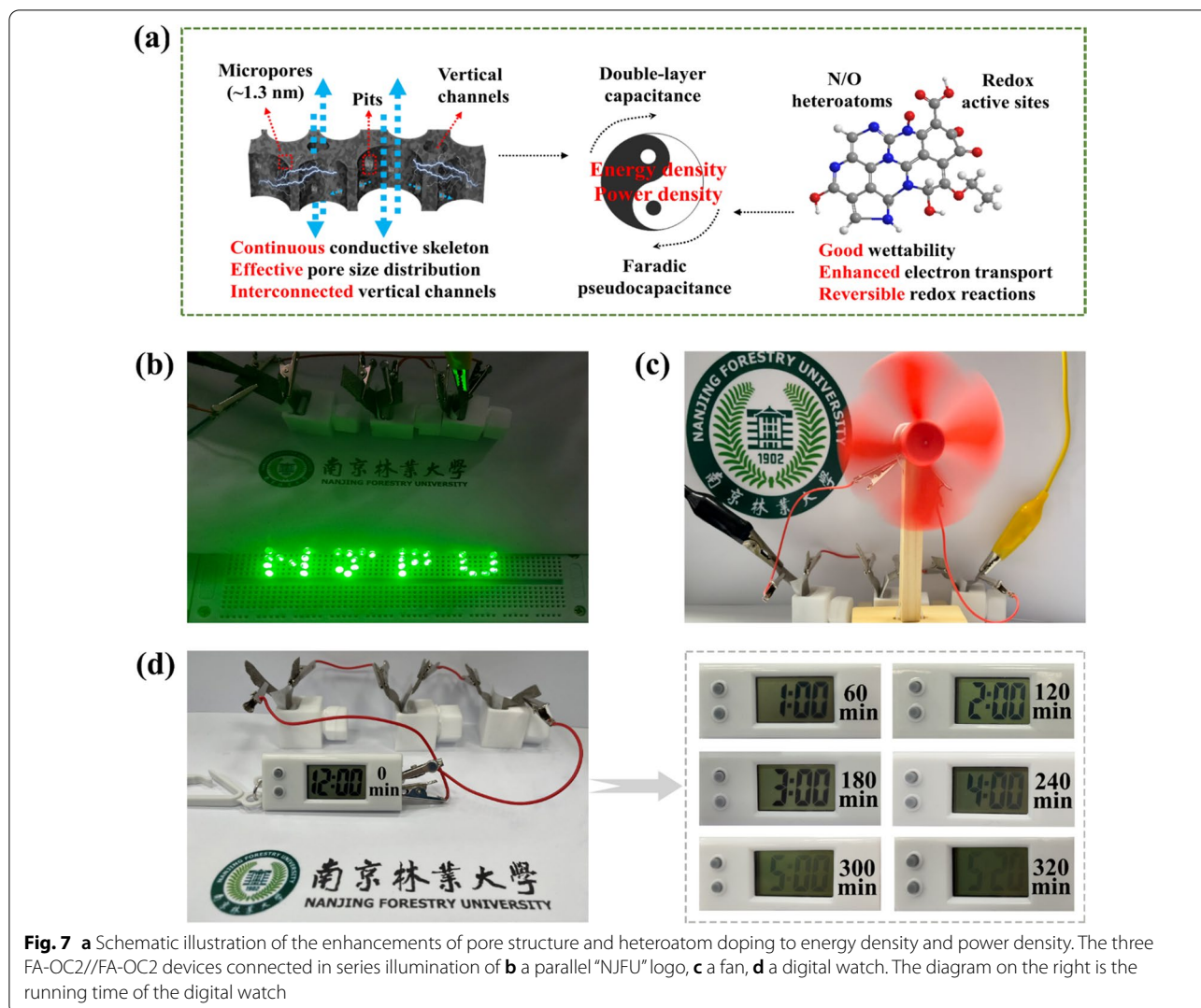
Fig. 7 a Schematic illustration of the enhancements of pore structure and heteroatom doping to energy density and power density. The three FA-OC2//FA-OC2 devices connected in series illumination of **b** a parallel "NJFU" logo, **c** a fan, **d** a digital watch. The diagram on the right is the running time of the digital watch

that the N/O-doped carbon materials possessed sustainable capacitive energy storage capability. The uniform self-supporting structure not only provided the homogeneous distribution of electrons and electrolyte ions along the thickness direction but in the whole monoliths, which ensured the stable electrochemical reaction and further improved the capacitive property. Hence, the three tandem all-carbon devices were capable to power a fan (Fig. 7b), illuminate a parallel "NJFU" logo (Fig. 7c) made up of 34 green light-emitting diodes (LEDs, 3 V), and run the digital watch for more than 5 h (Fig. 7d), revealing their practical application potential.

4 Conclusion

In summary, this work developed a self-standing carbon electrode with commercial-level active mass-loading (~ 40 mg cm^{-2}) and large active mass layer thickness (~ 800 μm) from basswood. Owing to the well-designed synthesis method, the carbon electrode possesses well conductive skeleton, abundant N/O dopants, and self-standing 3D porous structure. The synergistic effects from the low electrical resistance, optimal doping and free-standing porous structure significantly enhance the capacitive performance. As a result, the high areal/gravimetric/volumetric/SSA-normalized capacitances (6538.5 mF cm^{-2}, 223.9 F g^{-1}, 81.7 F cm^{-3} and 177.4 μF cm^{-2} at 2 mA cm^{-2} (0.05 A g^{-1})), the good rate capability (3821.2 mF cm^{-2}, 130.9 F g^{-1} and 47.8 F cm^{-3} at 500 mA cm^{-2} (12.50 A g^{-1})) and cycling stability ($\sim 94.3\%$ after 20,000 cycles at 500 mA cm^{-2}) are realized in the three-electrode configuration. The assembled symmetric supercapacitors deliver the specific capacitance of 5037.5 mF cm^{-2} (172.5 F g^{-1} and 63 F cm^{-3}) at 2 mA cm^{-2}, with the corresponding

energy density of 0.65 mWh cm^{-2} (22.44 Wh kg^{-1}, 8.15 mWh cm^{-3}). Furthermore, the three tandem all-carbon supercapacitors are capable of powering typical electronic devices including a fan, a parallel "NJFU" logo made up by 34 green light-emitting diodes (LEDs, 3 V), and a digital watch for proper time, revealing their practical application potential. This study not only develops a highly effective commercial-level active mass-loading electrode material for supercapacitors, but also inspires the utilization of sustainable biomass for energy-related applications.

Supplementary Information

The online version contains supplementary material available at https://doi.org/10.1007/s42773-022-00176-9.

> **Additional file 1.** Supplementary figures and tables.

Authors contributions
BY: Conceptualization, methodology, validation, formal analysis, investigation, resources, data curation, visualization, writing-original draft, writing-review and editing. JZ: Investigation, data curation, writing-review and editing. LF: Investigation, data curation, writing-review and editing. CD: Conceptualization, methodology, validation, supervision, project administration, writing-review and editing. SJ: Supervision, project administration, writing—review and editing. WY: Conceptualization, methodology, validation, formal analysis, resources, supervision, project administration, writing—review and editing, funding acquisition. YW: Investigation, data curation, writing—review and editing. SJ: Supervision, project administration, writing—review and editing. SH: Conceptualization, methodology, validation, formal analysis, resources, supervision, project administration, writing—review and editing, funding acquisition. WC: Project administration, writing—review and editing, funding acquisition. All authors read and approved the final manuscript.

Availability of data and materials
The raw and processed data required to reproduce the results of our work are available on reasonable request from the first author [Bing Yan].

Declarations

Competing interests
The authors declare that they have no known competing financial interests or personal relationships that could have appeared to influence the work reported in this paper.

Author details
[1] International Innovation Center for Forest Chemicals and Materials, Co-Innovation Center of Efficient Processing and Utilization of Forest Resources, College of Materials Science and Engineering, Nanjing Forestry University, Nanjing 210037, China. [2] State Key Laboratory of Electroanalytical Chemistry, Changchun Institute of Applied Chemistry, Chinese Academy of Sciences, Changchun 130022, Jilin, People's Republic of China. [3] Department of Mechanical and Mechatronics Engineering Waterloo Institute of Nanotechnology, University of Waterloo, Waterloo, ON N2L 3G1, Canada. [4] Fujian Key Laboratory of Eco-Industrial Green Technology, College of Ecology and Resources Engineering, Wuyi University, Wuyishan 354300, China. [5] University of Science and Technology of China, Hefei 230026, People's Republic of China.

References
Augustyn V, Simon P, Dunn B (2014) Pseudocapacitive oxide materials for high-rate electrochemical energy storage. Energy Environ Sci 7(5):1597. https://doi.org/10.1039/c3ee44164d

Boyce AM, Cumming DJ, Huang C, Zankowski SP, Grant PS, Brett DJL, Shearing PR (2021) Design of scalable, next-generation thick electrodes: opportunities and challenges. ACS Nano 15(12):18624–18632. https://doi.org/10.1021/acsnano.1c09687

Chang L, Hu YH (2019) Breakthroughs in designing commercial-level mass-loading graphene electrodes for electrochemical double-layer capacitors. Matter 1(3):596–620. https://doi.org/10.1016/j.matt.2019.06.016

Chen CJ, Zhang Y, Li Y, Dai JQ, Song JW, Yao YG, Gong YH, Kierzewski I, Xie J, Hu LB (2017) All-wood, low tortuosity, aqueous, biodegradable supercapacitors with ultra-high capacitance. Energy Environ Sci 10(2):538–545. https://doi.org/10.1039/c6ee03716j

Chen C, Kuang Y, Zhu S, Burgert I, Keplinger T, Gong A, Li T, Berglund L, Eichhorn SJ, Hu L (2020) Structure-property-function relationships of natural and engineered wood. Nat Rev Mater 5:642–666. https://doi.org/10.1038/s41578-020-0195-z

Chen L, Cao S, Huang L, Wu H, Hu H, Liu K, Lin S (2021a) Development of bamboo cellulose preparation and its functionalization. J for Eng 6(4):1–13. https://doi.org/10.13360/j.issn.2096-1359.202104011

Chen R, Ling H, Huang Q, Yang Y, Wang X (2021b) Interface engineering on cellulose-based flexible electrode enables high mass loading wearable supercapacitor with ultrahigh capacitance and energy density. Small 18(9):e2106356. https://doi.org/10.1002/smll.202106356

Chen Y, Li S, Li X, Mei C, Zheng J, Shiju E, Duan G, Liu K, Jiang S (2021c) Liquid transport and real-time dye purification via lotus petiole-inspired long-range-ordered anisotropic cellulose nanofibril aerogels. ACS Nano 15(12):20666–20677. https://doi.org/10.1021/acsnano.1c10093

Chen L, Wang F, Tian Z, Guo H, Cai C, Wu Q, Du H, Liu K, Hao Z, He S, Duan G, Jiang S (2022) Wood-derived high-mass-loading MnO$_2$ composite carbon electrode enabling high energy density and high-rate supercapacitor. Small 18:e2201307. https://doi.org/10.1002/smll.202201307

Daikopoulos C, Georgiou Y, Bourlinos AB, Baikousi M, Karakassides MA, Zboril R, Steriotis TA, Deligiannakis Y (2014) Arsenite remediation by an amine-rich graphitic carbon nitride synthesized by a novel low-temperature method. Chem Eng J 256:347–355. https://doi.org/10.1016/j.cej.2014.06.045

Ding Z, Trouillet V, Dsoke S (2019) Are functional groups beneficial or harmful on the electrochemical performance of activated carbon electrodes? J Electrochem Soc 166(6):A1004–A1014. https://doi.org/10.1149/2.0451906jes

Ding CF, Liu TY, Yan XD, Huang LB, Ryu S, Lan JL, Yu YH, Zhong WH, Yang XP (2020) An ultra-microporous carbon material boosting integrated capacitance for cellulose-based supercapacitors. Nano-Micro Lett 12(1):63. https://doi.org/10.1007/s40820-020-0393-7

Dong Y, Zhu J, Li Q, Zhang S, Song H, Jia D (2020) Carbon materials for high mass-loading supercapacitors: filling the gap between new materials and practical applications. J Mater Chem A 8(42):21930–21946. https://doi.org/10.1039/d0ta08265a

Du YF, Sun GH, Li Y, Cheng JY, Chen JP, Song G, Kong QQ, Xie LJ, Chen CM (2021) Pre-oxidation of lignin precursors for hard carbon anode with boosted lithium-ion storage capacity. Carbon 178:243–255. https://doi.org/10.1016/j.carbon.2021.03.016

Dubey R, Zwahlen MD, Shynkarenko Y, Yakunin S, Fuerst A, Kovalenko MV, Kravchyk KV (2020) Laser patterning of high-mass-loading graphite anodes for high-performance Li-Ion Batteries. Batter Supercaps 4(3):464–468. https://doi.org/10.1002/batt.202000253

Eliad L, Salitra G, Soffer A, Aurbach D (2001) Ion sieving effects in the electrical double layer of porous carbon electrodes: estimating effective ion size in

electrolytic solutions. J Phys Chem B 105(29):6880–6887. https://doi.org/10.1021/jp010086y

Ghosh S, Barg S, Jeong SM, Ostrikov K (2020) Heteroatom-doped and oxygen-functionalized nanocarbons for high-performance supercapacitors. Adv Energy Mater 10(32):2001239. https://doi.org/10.1002/aenm.202001239

González-Arias J, Sánchez ME, Cara-Jiménez J, Baena-Moreno FM, Zhang Z (2021) Hydrothermal carbonization of biomass and waste: a review. Environ Chem Lett 20(1):211–221. https://doi.org/10.1007/s10311-021-01311-x

Govind Raj K, Joy PA (2017) Role of localized graphitization on the electrical and magnetic properties of activated carbon. J Am Ceram Soc 100(11):5151–5161. https://doi.org/10.1111/jace.15035

Guo B, Ma R, Li Z, Guo S, Luo J, Yang M, Liu Q, Thomas T, Wang J (2020) Hierarchical N-doped porous carbons for Zn-air batteries and supercapacitors. Nano-Micro Lett 12(1):20. https://doi.org/10.1007/s40820-019-0364-z

Guo W, Yu C, Li S, Qiu J (2021) Toward commercial-level mass-loading electrodes for supercapacitors: opportunities, challenges and perspectives. Energy Environ Sci 14(2):576–601. https://doi.org/10.1039/d0ee02649b

Han M, Wang X, Chen C, Zou M, Niu Z, Yang Q-H, Cao A, Song L, Chen J, Xie S (2018) All-solid-state supercapacitors with superior compressive strength and volumetric capacitance. Energy Storage Mater 13:119–126. https://doi.org/10.1016/j.ensm.2018.01.007

He J, Zhang D, Wang Y, Zhang J, Yang B, Shi H, Wang K, Wang Y (2020) Biomass-derived porous carbons with tailored graphitization degree and pore size distribution for supercapacitors with ultra-high rate capability. Appl Surf Sci 515:146020. https://doi.org/10.1016/j.apsusc.2020.146020

Hou L, Yang W, Li Y, Wang P, Jiang B, Xu C, Zhang C, Huang G, Yang F, Li Y (2021) Dual-template endowing N, O co-doped hierarchically porous carbon from potassium citrate with high capacitance and rate capability for supercapacitors. Chem Eng J 417:129289. https://doi.org/10.1016/j.cej.2021.129289

Huang J, Zhao B, Liu T, Mou J, Jiang Z, Liu J, Li H, Liu M (2019a) Wood-derived materials for advanced electrochemical energy storage devices. Adv Funct Mater 29(31):1902255. https://doi.org/10.1002/adfm.201902255

Huang T, Chu X, Cai S, Yang Q, Chen H, Liu Y, Gopalsamy K, Xu Z, Gao W, Gao C (2019b) Tri-high designed graphene electrodes for long cycle-life supercapacitors with high mass loading. Energy Storage Mater 17:349–357. https://doi.org/10.1016/j.ensm.2018.07.001

Jjagwe J, Olupot PW, Menya E, Kalibbala HM (2021) Synthesis and application of granular activated carbon from biomass waste materials for water treatment: a review. J Bioresour Bioprod 6(4):292–322. https://doi.org/10.1016/j.jobab.2021.03.003

Katsuyama Y, Haba N, Kobayashi H, Iwase K, Kudo A, Honma I, Kaner RB (2022) Macro- and nano-porous 3D-hierarchical carbon lattices for extraordinarily high capacitance supercapacitors. Adv Funct Mater 32(24):2201544. https://doi.org/10.1002/adfm.202201544

Kim C, Zhu C, Aoki Y, Habazaki H (2019) Heteroatom-doped porous carbon with tunable pore structure and high specific surface area for high performance supercapacitors. Electrochim Acta 314:173–187. https://doi.org/10.1016/j.electacta.2019.05.074

Kuang Y, Chen C, Kirsch D, Hu L (2019) Thick electrode batteries: principles, opportunities, and challenges. Adv Energy Mater 9(33):1901457. https://doi.org/10.1002/aenm.201901457

Lachos-Perez D, Cesar Torres-Mayanga P, Abaide ER, Zabot GL, De Castilhos F (2022) Hydrothermal carbonization and liquefaction: differences, progress, challenges, and opportunities. Bioresour Technol 343:126084. https://doi.org/10.1016/j.biortech.2021.126084

Leng E, Guo Y, Chen J, Liu S, Jiaqiang E, Xue Y (2022) A comprehensive review on lignin pyrolysis: mechanism, modeling and the effects of inherent metals in biomass. Fuel 309:122102. https://doi.org/10.1016/j.fuel.2021.122102

Li Z, Wang D, Li H, Ma M, Zhang Y, Yan Z, Agnoli S, Zhang G, Sun X (2022) Single-atom Zn for boosting supercapacitor performance. Nano Res 15(3):1715–1724. https://doi.org/10.1007/s12274-021-3839-4

Lin X, Liu Y, Tan H, Zhang B (2020) Advanced lignin-derived hard carbon for Na-ion batteries and a comparison with Li and K ion storage. Carbon 157:316–323. https://doi.org/10.1016/j.carbon.2019.10.045

Lin S, Wang Y, Chen Y, Cai Z, Xiao J, Muhmood T, Hu X (2021) 3D ordered porous nanostructure confers fast charge transfer rate and reduces the electrode polarization in thick electrode. Small 18(7):e2104224. https://doi.org/10.1002/smll.202104224

Liu K, Xu J, Wang Y, Qian M, Zhao W, Zeng Y, Huang F (2019a) Boron and nitrogen Co-doped trimodal-porous wood-derived carbon for boosting capacitive performance. Energy Technol 8(1):1900950. https://doi.org/10.1002/ente.201900950

Liu T, Zhou Z, Guo Y, Guo D, Liu G (2019b) Block copolymer derived uniform mesopores enable ultrafast electron and ion transport at high mass loadings. Nat Commun 10(1):675. https://doi.org/10.1038/s41467-019-08644-w

Liu HL, Xie YX, Liu JB, Moon K-s, Lu LS, Lin ZR, Yuan W, Shen CW, Zang XN, Lin LW, Tang Y, Wong CP (2020) Laser-induced and KOH-activated 3D graphene: a flexible activated electrode fabricated via direct laser writing for in-plane micro-supercapacitors. Chem Eng J 393:124672. https://doi.org/10.1016/j.cej.2020.124672

Liu Y, Wu X, Guo X, Lee K, Sun Q, Li X, Zhang C, Wang Z, Hu J, Zhu Y, Leung MKH, Zhu Z (2021) Modulate FeCo nanoparticle in situ growth on carbon matrix for high-performance oxygen catalysts. Mater Today Energy 19:100610. https://doi.org/10.1016/j.mtener.2020.100610

Liu S, Zhao Z, Jin L, Sun J, Jiao C, Wang Q (2022a) Nitrogen-doped carbon networks with consecutive conductive pathways from a facile competitive carbonization-etching strategy for high-performance energy storage. Small 18:2104375. https://doi.org/10.1002/smll.202104375

Liu Z, Duan C, Dou S, Yuan Q, Xu J, Liu WD, Chen Y (2022b) Ultrafast porous carbon activation promises high-energy density supercapacitors. Small 18:e2200954. https://doi.org/10.1002/smll.2022b00954

Lu H, Yang C, Chen J, Li J, Jin H, Wang J, Wang S (2020) Tailoring hierarchically porous nitrogen-, sulfur-codoped carbon for high-performance supercapacitors and oxygen reduction. Small 16(17):e1906584. https://doi.org/10.1002/smll.201906584

Lü F, Lu X, Li S, Zhang H, Shao L, He P (2022) Dozens-fold improvement of biochar redox properties by KOH activation. Chem Eng J 429:132203. https://doi.org/10.1016/j.cej.2021.132203

Ma Y, Yao D, Liang H, Yin J, Xia Y, Zuo K, Zeng Y-P (2020) Ultra-thick wood biochar monoliths with hierarchically porous structure from cotton rose for electrochemical capacitor electrodes. Electrochim Acta 352:136452. https://doi.org/10.1016/j.electacta.2020.136452

Oh J, Park S, Jang D, Shin Y, Lim D, Park S (2019) Metal-free N-doped carbon blacks as excellent electrocatalysts for oxygen reduction reactions. Carbon 145:481–487. https://doi.org/10.1016/j.carbon.2019.01.056

Peng J, Liu X, Bao Z (2019) Pyrolysis behavior of basswood by TG. IOP Conf Ser: Mater Sci Eng 490:022051. https://doi.org/10.1088/1757-899x/490/2/022051

Plaza-Rivera CO, Walker BA, Tran NX, Viggiano RP, Dornbusch DA, Wu JJ, Connell JW, Lin Y (2020) Dry pressing neat active materials into ultrahigh mass loading sandwich cathodes enabled by holey graphene scaffold. ACS Appl Energy Mater 3(7):6374–6382. https://doi.org/10.1021/acsaem.0c00582

Qing Y, Liao Y, Liu J, Tian C, Xu H, Wu Y (2021) Research progress of wood-derived energy storage materials. J for Eng 6(05):1–13. https://doi.org/10.13360/j.issn.2096-1359.202012046

Ran F, Yang X, Xu X, Li S, Liu Y, Shao L (2021) Green activation of sustainable resources to synthesize nitrogen-doped oxygen-riched porous carbon nanosheets towards high-performance supercapacitor. Chem Eng J 412:128673. https://doi.org/10.1016/j.cej.2021.128673

Shang J, Lin J, Zhao G (2018) Preparation and characterization of wood-based pre-oxidized precursors and activated carbon microspheres. BioResources 13:7983–7997. https://doi.org/10.15376/biores.13.4.7983-7997

Su X, Ye C, Li X, Guo M, Cao R, Ni K, Zhu Y (2022) Heterogeneous stacking carbon films for optimized supercapacitor performance. Energy Storage Mater 50:365–372. https://doi.org/10.1016/j.ensm.2022.05.020

Sun X, Lu H, Rufford TE, Gaddam RR, Duignan TT, Fan X, Zhao XS (2019) A flexible graphene-carbon fiber composite electrode with high surface area-normalized capacitance. Sustainable Energy Fuels 3(7):1827–1832. https://doi.org/10.1039/c9se00099b

Sun C, Guo Z, Zhou M, Li X, Cai Z, Ge F (2021) Heteroatoms-doped porous carbon electrodes with three-dimensional self-supporting structure derived from cotton fabric for high-performance wearable supercapacitors. J Power Sources 482:228934. https://doi.org/10.1016/j.jpowsour.2020.228934

Tang Z, Pei Z, Wang Z, Li H, Zeng J, Ruan Z, Huang Y, Zhu M, Xue Q, Yu J, Zhi C (2018) Highly anisotropic, multichannel wood carbon with optimized

heteroatom doping for supercapacitor and oxygen reduction reaction. Carbon 130:532–543. https://doi.org/10.1016/j.carbon.2018.01.055

Teng W, Zhou Q, Wang X, Che H, Du Y, Hu P, Li H, Wang J (2021) Biotemplating preparation of N, O-codoped hierarchically porous carbon for high-performance supercapacitors. Appl Surf Sci 566:150613. https://doi.org/10.1016/j.apsusc.2021.150613

Thommes M, Kaneko K, Neimark AV, Olivier JP, Rodriguez-Reinoso F, Rouquerol J, Sing KSW (2015) Physisorption of gases, with special reference to the evaluation of surface area and pore size distribution (IUPAC Technical Report). Pure Appl Chem 87(9–10):1051–1069. https://doi.org/10.1515/pac-2014-1117

Thongsai N, Hrimchum K, Aussawasathien D (2021) Carbon fiber mat from palm-kernel-shell lignin/polyacrylonitrile as intrinsic-doping electrode in supercapacitor. Sustain Mater Technol 30:e00341. https://doi.org/10.1016/j.susmat.2021.e00341

Tian W, Zhu J, Dong Y, Zhao J, Li J, Guo N, Lin H, Zhang S, Jia D (2020) Micelle-induced assembly of graphene quantum dots into conductive porous carbon for high rate supercapacitor electrodes at high mass loadings. Carbon 161:89–96. https://doi.org/10.1016/j.carbon.2020.01.044

Wabo SG, Klepel O (2021) Nitrogen release and pore formation through KOH activation of nitrogen-doped carbon materials: an evaluation of the literature. Carbon Lett 31(4):581–592. https://doi.org/10.1007/s42823-021-00252-3

Wang Y, Lin X, Liu T, Chen H, Chen S, Jiang Z, Liu J, Huang J, Liu M (2018) Wood-derived hierarchically porous electrodes for high-performance all-solid-state supercapacitors. Adv Funct Mater 28(52):1806207. https://doi.org/10.1002/adfm.201806207

Wang Y, Hu YJ, Hao X, Peng P, Shi JY, Peng F, Sun RC (2020) Hydrothermal synthesis and applications of advanced carbonaceous materials from biomass: a review. Adv Compos Hybrid Mater 3(3):267–284. https://doi.org/10.1007/s42114-020-00158-0

Wang C, Yan B, Zheng J, Feng L, Chen Z, Zhang Q, Liao T, Chen J, Jiang S, Du C, He S (2021a) Recent progress in template-assisted synthesis of porous carbons for supercapacitors. Adv Powder Mater 1(2):100018. https://doi.org/10.1016/j.apmate.2021.11.005

Wang F, Cheong JY, He Q, Duan G, He S, Zhang L, Zhao Y, Kim I-D, Jiang S (2021b) Phosphorus-doped thick carbon electrode for high-energy density and long-life supercapacitors. Chem Eng J 414:128767. https://doi.org/10.1016/j.cej.2021.128767

Wang F, Cheong JY, Lee J, Ahn J, Duan G, Chen H, Zhang Q, Kim ID, Jiang S (2021c) Pyrolysis of enzymolysis-treated wood: hierarchically assembled porous carbon electrode for advanced energy storage devices. Adv Funct Mater 31(31):2101077. https://doi.org/10.1002/adfm.202101077

Wang F, Liu X, Duan G, Yang H, Cheong JY, Lee J, Ahn J, Zhang Q, He S, Han J, Zhao Y, Kim ID, Jiang S (2021d) Wood-derived, conductivity and hierarchical pore integrated thick electrode enabling high areal/volumetric energy density for hybrid capacitors. Small 17:2102532. https://doi.org/10.1002/smll.202102532

Wang F, Zhang L, Zhang Q, Yang J, Duan G, Xu W, Yang F, Jiang S (2021e) Electrode thickness design toward bulk energy storage devices with high areal/volumetric energy density. Appl Energy 289:116734. https://doi.org/10.1016/j.apenergy.2021.116734

Wang G, Lu Z, Li Y, Li L, Ji L, Feteira A, Zhou D, Wang D, Zhang S, Reaney IM (2021f) Electroceramics for high-energy density capacitors: current status and future perspectives. Chem Rev 121(10):6124–6172. https://doi.org/10.1021/acs.chemrev.0c01264

Wang R, Zhou X, Xu T, Bian H, Dai H (2021g) Research progress on the preparation of lignin-derived carbon dots and graphene quantum dots. J for Eng 6(01):29–37. https://doi.org/10.13360/j.issn.2096-1359.202001007

Wang F, Chen L, He S, Zhang Q, Liu K, Han X, Duan G, Jiang S (2022a) Design of wood-derived anisotropic structural carbon electrode for high-performance supercapacitor. Wood Sci Technol. https://doi.org/10.1007/s00226-022-01389-8

Wang M, Han K, Qi J, Teng Z, Zhang J, Li M (2022b) Study on performance and charging dynamics of N/O codoped layered porous carbons derived from L-tyrosine for supercapacitors. Appl Surf Sci 578:151888. https://doi.org/10.1016/j.apsusc.2021.151888

Wei L, Yushin G (2012) Nanostructured activated carbons from natural precursors for electrical double layer capacitors. Nano Energy 1(4):552–565. https://doi.org/10.1016/j.nanoen.2012.05.002

Wu S, Chen G, Kim NY, Ni K, Zeng W, Zhao Y, Tao Z, Ji H, Lee Z, Zhu Y (2016) Creating pores on graphene platelets by low-temperature KOH activation for enhanced electrochemical performance. Small 12(17):2376–2384. https://doi.org/10.1002/smll.201503855

Wu J, Zhang X, Ju Z, Wang L, Hui Z, Mayilvahanan K, Takeuchi KJ, Marschilok AC, West AC, Takeuchi ES, Yu G (2021) From fundamental understanding to engineering design of high-performance thick electrodes for scalable energy-storage systems. Adv Mater 33(26):e2101275. https://doi.org/10.1002/adma.202101275

Xia J, Zhang N, Chong S, Li D, Chen Y, Sun C (2018) Three-dimensional porous graphene-like sheets synthesized from biocarbon via low-temperature graphitization for a supercapacitor. Green Chem 20(3):694–700. https://doi.org/10.1039/c7gc03426a

Xia Z, Li J, Zhang J, Zhang X, Zheng X, Zhang J (2020) Processing and valorization of cellulose, lignin and lignocellulose using ionic liquids. J Bioresour Bioprod 5(2):79–95. https://doi.org/10.1016/j.jobab.2020.04.001

Xiao J, Li H, Zhang H, He S, Zhang Q, Liu K, Jiang S, Duan G, Zhang K (2022) Nanocellulose and its derived composite electrodes toward supercapacitors: fabrication, properties, and challenges. J Bioresour Bioprod. https://doi.org/10.1016/j.jobab.2022.05.003

Xu L, Xi Y, Li W, Hua Z, Peng J, Hu J, Zhou J-J, Zhang P, Wang J, Wang W, Ding H, Wang W, Ji W, Yang Y, Xu X, Chen L, Li X (2021) 3D frame-like architecture of N-C-incorporated mixed metal phosphide boosting ultrahigh energy density pouch-type supercapacitors. Nano Energy 91:106630. https://doi.org/10.1016/j.nanoen.2021.106630

Yan J, Wang Q, Wei T, Fan Z (2014) Recent advances in design and fabrication of electrochemical supercapacitors with high energy densities. Adv Energy Mater 4(4):1300816. https://doi.org/10.1002/aenm.201300816

Yang L, Huang N, Luo C, Yu H, Sun P, Lv X, Sun X (2021) Atomically dispersed and nanoscaled Co species embedded in micro-/mesoporous carbon nanosheet/nanotube architecture with enhanced oxygen reduction and evolution bifunction for Zn-Air batteries. Chem Eng J 404:127112. https://doi.org/10.1016/j.cej.2020.127112

Yu Y, Peng H, Du C, Zhang Y, Wan L, Chen J, Xiong X, Xie M, Wang X (2022) Alkaline-carbonate-templated carbon: effect of template nature on morphology, oxygen species and supercapacitor performances. Appl Surf Sci 575:151771. https://doi.org/10.1016/j.apsusc.2021.151771

Zhang S, Tsuzuki S, Ueno K, Dokko K, Watanabe M (2015) Upper limit of nitrogen content in carbon materials. Angew Chem Int Ed Engl 54(4):1302–1306. https://doi.org/10.1002/anie.201410234

Zhang S, Wu CL, Wu W, Zhou C, Xi ZW, Deng YY, Wang X, Quan P, Li XJ, Luo YF (2019a) High performance flexible supercapacitors based on porous wood carbon slices derived from Chinese fir wood scraps. J Power Sources 424:1–7. https://doi.org/10.1016/j.jpowsour.2019.03.100

Zhang W, Liang S, Fang G, Yang Y, Zhou J (2019b) Ultra-high mass-loading cathode for aqueous zinc-ion battery based on graphene-wrapped aluminum vanadate nanobelts. Nano-Micro Lett 11(1):69. https://doi.org/10.1007/s40820-019-0300-2

Zhang Y, Zhou K, Qiu Y, Xia L, Xia Z, Zhang K, Fu Q (2021) Strongly emissive formamide-derived N-doped carbon dots embedded Eu(III)-based metal-organic frameworks as a ratiometric fluorescent probe for ultrasensitive and visual quantitative detection of Ag$^+$. Sens Actuators, B 339:129922. https://doi.org/10.1016/j.snb.2021.129922

Zhao Z, Sun M, Chen W, Liu Y, Zhang L, Dongfang N, Ruan Y, Zhang J, Wang P, Dong L, Xia Y, Lu H (2019) Sandwich, vertical-channeled thick electrodes with high rate and cycle performance. Adv Funct Mater 29(16):1809196. https://doi.org/10.1002/adfm.201809196

Zhao Y, Dong C, Sheng L, Xiao Z, Jiang L, Li X, Jiang M, Shi J (2020) Heteroatom-doped pillared porous carbon architectures with ultrafast electron and ion transport capabilities under high mass loadings for high-rate supercapacitors. ACS Sustain Chem Eng 8(23):8664–8674. https://doi.org/10.1021/acssuschemeng.0c01661

Zhao X, He D, You B (2022) Laser engraving and punching of graphene films as flexible all-solid-state planar micro-supercapacitor electrodes. Mater Today Sustainability 17:100096. https://doi.org/10.1016/j.mtsust.2021.100096

Zheng S, Wang Q, Hou Y, Li L, Tao Z (2021a) Recent progress and strate-gies toward high performance zinc-organic batteries. J Energy Chem 63:87–112. https://doi.org/10.1016/j.jechem.2021.07.027

Zheng S, Zhang J, Deng H, Du Y, Shi X (2021b) Chitin derived nitrogen-doped porous carbons with ultrahigh specific surface area and tailored hierar-chical porosity for high performance supercapacitors. J Bioresour Bioprod 6(2):142–151. https://doi.org/10.1016/j.jobab.2021.02.002

Zheng W, Halim J, Sun Z, Rosen J, Barsoum MW (2021c) MXene-manganese oxides aqueous asymmetric supercapacitors with high mass load-ings, high cell voltages and slow self-discharge. Energy Storage Mater 38:438–446. https://doi.org/10.1016/j.ensm.2021.03.011

Zhong L, Jiang C, Zheng M, Peng X, Liu T, Xi S, Chi X, Zhang Q, Gu L, Zhang S, Shi G, Zhang L, Wu K, Chen Z, Li T, Dahbi M, Alami J, Amine K, Lu J (2021) Wood carbon based single-atom catalyst for rechargeable Zn–air batter-ies. ACS Energy Lett 6(10):3624–3633. https://doi.org/10.1021/acsenergyl ett.1c01678

Zuliani JE, Tong S, Jia CQ, Kirk DW (2018) Contribution of surface oxygen groups to the measured capacitance of porous carbon supercapacitors. J Power Sources 395:271–279. https://doi.org/10.1016/j.jpowsour.2018. 05.046